Impact of aerosol processing in the transition of a stratocumulus cloud system to open cells: A comparison of Lagrangian and bin microphysics schemes in LES

Kamal Kant Chandrakar [1] **and Hugh Morrison** [1]

[1]NSF National Center for Atmospheric Research, Boulder, CO 80307

Key Points:

- Substantial aerosol scavenging and physical processing by clouds, affecting drizzle formation, is simulated using Lagrangian microphysics.
- Reduced aerosol concentration and size distribution changes impact aerosol removal via precipitation and time to open cell formation.
- A positive cloud-aerosol-rain feedback accelerates rain formation and aerosol removal using the Lagrangian compared to bin scheme.

Corresponding author: Kamal Kant Chandrakar, kkchandr@ucar.edu

Abstract

Stratocumulus clouds, a key component of global climate, are sensitive to aerosol properties. Aerosol-cloud-precipitation interactions in these clouds influence their closed-to-open cell dynamical transition and hence cloud cover and radiative forcing. This study uses large-eddy simulations with Lagrangian super-particle and bin microphysics schemes to investigate impacts of aerosol scavenging and physical processing by clouds on drizzle initiation and the cellular transition process. The simulation using Lagrangian microphysics with explicit representation of cloud-borne aerosol and scavenging shows significant aerosol processing that impacts precipitation generation and consequently the closed-to-open cell transition. Sensitivity simulations using the bin scheme and their comparison with the Lagrangian microphysics simulation suggest that reduced aerosol concentration due to scavenging is a primary microphysical catalyst for enhanced precipitation using the Lagrangian scheme. However, changes in the aerosol distribution shape through processing also contribute appreciably to the differences in precipitation rate. Thus, both aerosol scavenging and processing drive earlier rain formation and the transition to open cells in the simulation with Lagrangian microphysics. This study also highlights a shortcoming of Eulerian bin microphysics producing smaller mean drop radius and cloud water mixing ratios owing to numerical diffusion. Initially larger mean radius and cloud mixing ratios using the Lagrangian scheme induce faster rain development compared to the bin scheme. A positive feedback in turn accelerates aerosol removal and further rain production using the Lagrangian scheme and, consequently, reduced cloud droplet number, increased mean size, and increased droplet spectral width.

Plain Language Summary

Stratocumulus clouds reflect substantial solar radiation due to their extensive coverage and are therefore a critical component of regional and global climate. Aerosol particles and their two-way interactions with these clouds impact drizzle formation and their transition to a less reflective open-cellular cloud structure. In this study, we show that both the reduction of aerosol concentration and changes in aerosol particle sizes due to their interactions with cloud and drizzle drops impact precipitation formation and the time required to transition to an open-cell structure. Such aerosol-cloud interactions are highly simplified in commonly used cloud models due to the difficulty of tracking the solute mass of aerosols in individual cloud drops. A newer modeling approach called the Lagrangian "super-doplet" method is a state-of-the-art tool that can better represent aerosol-cloud interactions by explicitly tracking aerosol properties in cloud and drizzle drops and reducing other numerical errors. We show that limitations of traditional cloud models, particularly in how they represent aerosol scavenging and processing, affect the predicted micro-scale cloud properties. This leads to delayed formation of rain and the transition to an open cellular cloud structure compared to the simulation using the super-particle modeling approach.

1 Introduction

Stratocumulus clouds significantly affect the earth's energy balance (Slingo, 1990). The mesoscale structure of boundary layer clouds, affecting cloud cover, is critical to their radiative forcing and precipitation formation. Aerosol-cloud-precipitation interactions in turn influence the mesoscale structure, dynamics, and lifetime of clouds. Aerosol impacts on marine low clouds are a key for global climate modeling (e.g., Zhang et al., 2016) and underlie the potential for marine cloud brightening to offset global warming (Latham et al., 2008; Diamond et al., 2022; Feingold et al., 2022). This study aims to elucidate aerosol-cloud-precipitation interactions in stratocumulus clouds using state-of-the-art large-eddy simulations (LES) with two different approaches for size-resolved representation of microphysics.

Aerosols induce changes to cloud microphysics (Twomey, 1974; Chandrakar et al., 2016), thereby influencing macroscopic cloud properties and processes (e.g., cloud thickness, precipitation formation, cloud cover, liquid water path, patterns of convection, radiative forcing, etc.) through various process interactions (Albrecht, 1989; Pincus & Baker, 1994; Ackerman et al., 2004; Wood, 2012; Glassmeier et al., 2021). Aerosol scavenging and processing in stratocumulus cloud systems can substantially influence their dynamical states. For example, precipitation suppression from aerosol loading can alter patterns of latent heating and evaporative cooling, in turn affecting the dynamics, turbulent kinetic energy (TKE), and entrainment rate (Wood, 2012). Indeed, modeling studies have suggested that the transformation of a cloud system from closed to open cells can occur merely from a reduced aerosol concentration (Wang & Feingold, 2009). Aerosols also influence cloud drop size distributions (DSDs), which could impact the entrainment rate directly through the settling-entrainment and evaporation-entrainment feedbacks, causing the liquid water path and cloud albedo to change (Ackerman et al., 2004; Bretherton et al., 2007; Hill et al., 2008). In a clean marine environment, the response of clouds to changes in aerosol concentration is expected to be more acute than in polluted conditions (Reutter et al., 2009; Chandrakar et al., 2017). A key question is, how do aerosol-cloud interactions with various associated feedbacks impact the stratocumulus transition to a cleaner state?

Clouds also affect aerosol properties and remove aerosol particles from the boundary layer by scavenging. Cloud condensation nuclei (CCN) activate cloud droplets, which can grow to drizzle sizes mainly through collision-coalescence and are removed through precipitation (a wet scavenging process). These in-cloud interactions may drive changes in aerosol composition and size due to chemical (gas diffusion and aqueous chemistry) as well as physical (diffusion/impaction of interstitial aerosol particles to droplets and droplet coagulation) processing (Hoppel et al., 1990; Bower et al., 1999; Pierce et al., 2015). Interstitial aerosols also grow through vapor deposition and coagulation (Seinfeld & Pandis, 1998). After evaporation of cloud and drizzle drops, the processed aerosols are again available as a CCN source but with altered properties (Hoppel et al., 1990; Pierce et al., 2015; Chandrakar, Morrison, & Witte, 2022; Hoffmann & Feingold, 2023). This modification of properties could make them more efficient CCN due to increased solute mass through the physical and chemical processing (Hudson et al., 2015), thereby affecting drizzle formation in stratocumulus clouds. Multiple cycles of aerosol processing are suggested to produce a bimodal aerosol size distribution shape as air masses are advected from the coast to the remote ocean (Hoppel et al., 1990). The activation scavenging of aerosols to cloud droplets depends on the degree of competition for water vapor (Goren & Rosenfeld, 2015; Chandrakar et al., 2017). Thus, as a cloud system gets cleaner through precipitation formation and wet scavenging, the scavenging rate could accelerate in a positive feedback loop, rapidly increasing the precipitation flux. Past studies (e.g., Rosenfeld et al., 2006; Wang & Feingold, 2009; Wood et al., 2011; Chandrakar, Morrison, & Witte, 2022) have shown that drizzle formation can impact mesoscale cloud properties and drive a transition in cloud cellular structure. Most earlier studies (e.g., Goren et al., 2019; Erfani et al., 2022) on this topic used bulk microphysics schemes, where the details of aerosol processing are highly parameterized and therefore uncertain. A microphysics scheme that can track aerosol properties inside and outside clouds/drizzle drops is needed to capture aerosol processing in clouds with greater fidelity.

Representation of aerosol-cloud-precipitation interactions, even in detailed process models, is a significant challenge. Aerosol scavenging and processing add substantial complexity to this problem. Eulerian microphysics schemes, both bulk and bin, have traditionally been used for past studies of the stratocumulus transition to open cells (e.g., Wang & Feingold, 2009; Mechem & Kogan, 2003; Berner et al., 2011; Duynkerke et al., 2004; Glassmeier & Feingold, 2017; Goren et al., 2019). While relatively computationally efficient, several limitations (discussed below) could affect the ability of these schemes to capture aerosol-cloud-precipitation interactions and their impact on macroscopic cloud

properties and mesoscale features. Lagrangian passive trajectory models with improved treatment of aerosols have also been used in the past for process-level studies of drizzle formation and aerosol-cloud interactions in stratocumulus (e.g., Feingold et al., 1999; Pinsky et al., 2008; Magaritz et al., 2009). However, these models neglected feedback between the dynamics and microphysics, used Eulerian bin schemes, and were mainly restricted to small two-dimensional domains.

With recent advances in computing power, LES using a mesoscale domain with detailed Lagrangian particle-based microphysics explicitly representing aerosol-cloud interactions is now feasible. This modeling setup can elucidate complex cloud-aerosol-precipitation-dynamics interactions with greater fidelity than models with traditional Eulerian bulk or bin microphysics schemes. Lagrangian particle-based schemes track "super-particles" in the modeled flow, each representing a multitude of real aerosol, cloud and rain particles. In this work, we use the Super-Droplet Method (SDM) Lagrangian scheme (Shima et al., 2009) in LES. Lagrangian particle-based schemes address key limitations in Eulerian bulk and bin schemes (Grabowski et al., 2019), particularly by their ability to track cloud-borne aerosols explicitly as well as by eliminating numerical diffusion of cloud and precipitation variables which is problematic for traditional Eulerian schemes (Morrison et al., 2018; Lee et al., 2021; Chandrakar, Morrison, Grabowski, & Bryan, 2022). A few recent studies (e.g., Andrejczuk et al., 2010; Dziekan et al., 2021; Chandrakar, Morrison, & Witte, 2022; Hoffmann & Feingold, 2023) demonstrated the potential of Lagrangian microphysics schemes in LES for simulating aerosol-cloud interactions in stratocumulus clouds. In this article, we investigate the role of aerosol scavenging and processing in the cellular transition of a stratocumulus cloud field using a Lagrangian super-particle scheme and compare results to those using an Eulerian bin scheme. Specifically, we investigate the following science questions:

- How do the scavenging and processing of aerosols by physical cloud processes impact the evolution of cloud microphysical properties and drizzle formation?
- How do aerosol scavenging and processing influence the transition from closed to open cells? What is the impact of aerosol processing on drizzle formation and the cellular transition relative to that of aerosol scavenging alone?
- Considering the limitations of bin schemes, how do simulations with a bin scheme evolve differently than those with SDM? How do cloud properties simulated using SDM and the bin scheme compare after the transition to open cells?

The rest of the manuscript is outlined as follows. Section 2 discusses the model, simulation setup, and sensitivity cases. In the results section (Sec. 3), the evolution of cloud properties during the cellular transition from the control SDM simulation is presented first to illustrate results using the most detailed representation of aerosol and cloud physical processes. Aerosol scavenging and processing during the cellular transition are discussed in Sec. 3.2, and the SDM and bin simulations are compared in Sec. 3.3. Finally, we summarize the significant findings and provide conclusions in Sec. 4.

2 Model Description and Case Setup

The current study uses CM1 (Cloud Model 1; Bryan & Fritsch, 2002) non-hydrostatic dynamical core in a LES configuration to simulate the DYCOMS-II RF02 drizzling stratocumulus case from Ackerman et al. (2009). A prognostic subgrid turbulent kinetic energy scheme (Deardorff, 1980) is used for subgrid closure. The Lagrangian super-droplet method (SDM, Shima et al., 2020) and the Eulerian Tel Aviv University (TAU) bin scheme (Tzivion et al., 1987; Feingold et al., 1988; Stevens et al., 1996) are used as microphysical models in CM1.

The SDM simulation has 128 super-particles on average per grid box representing aerosol, cloud, and rain particles. The Lagrangian transport equation of SDM uses a velocity field linearly interpolated to the location of each particle from the CM1 Eulerian wind field and a Lagrangian subgrid velocity associated with each particle driven by LES subgrid turbulence statistics (Chandrakar et al., 2021). SDM tracks solute mass in haze, cloud and rain drops. It explicitly represents the activation and wet growth of aerosols by accounting for curvature and solute effects in the condensation growth equation for all particles. SDM uses a stochastic collision-coalescence scheme (Shima et al., 2009) with the Hall coalescence kernel for drop coalescence. Impaction aerosol scavenging is represented using the Brownian coagulation kernel (Seinfeld & Pandis, 2016). There is no external aerosol source in the boundary layer (only internal sources through regeneration from drop evaporation and entrainment from the free troposphere) to simplify the investigation of the transition. See Chandrakar et al. (2021); Chandrakar, Morrison, Grabowski, and Bryan (2022) for more details of the CM1-SDM model.

Contrary to SDM, the version of TAU used here does not track the solute mass in cloud and rain drops. It tracks the water mass of haze aerosols but assumes a quasi-equilibrium wet radius following the Köhler curve. When droplets activate, they are placed in appropriate bins based on their critical radius. During evaporation, deactivated cloud droplets are placed in aerosol bins, which are re-filled up to the background (initial) aerosol concentration. The bins are re-filled starting with the smallest aerosol bin that is depleted relative to the background aerosol, and moving to progressively larger bins until all deactivated drops are transferred to aerosol during the time step. The aerosol size distribution in each LES grid cell is tracked using 20 logarithmically spaced bins. Cloud/rain drop size distributions are represented using 35 mass-doubling bins for number and mass mixing ratios (two-moment) with a minimum radius of 1.56 μm. Drop and aerosol bins are advected using the scalar advection scheme in CM1. TAU solves the stochastic collection equation as in (Tzivion et al., 1987) using the Hall kernel. Further details of CM1-TAU and CM1-SDM are given in (Chandrakar, Morrison, Grabowski, & Bryan, 2022), where they are compared in LES of a cumulus congestus cloud.

The case setup is the same as presented in Chandrakar, Morrison, and Witte (2022). The boundary layer is driven by constant surface latent and sensible heat fluxes (Ackerman et al., 2009) and a bulk longwave radiative cooling approach based Stevens et al. (2005). A uniform large-scale horizontal divergence is applied to represent subsidence. The initial wind shear is set to zero to simplify the setup and avoid the influence of shear on the mesoscale organization and transition to open cells. The simulation domain size is 50×25 km^2 horizontally and 1.5 km vertically with uniform 100 m horizontal and 5 m vertical grid spacings. A relatively fine vertical grid spacing is used to represent entrainment and cloud processes better (Mellado et al., 2018), and coarser horizontal grid spacing is necessary for the feasibility of using a mesoscale domain. These grid spacings are finer than some previous studies of the cellular transition (e.g., Goren et al., 2019) but the same as our recent work in Chandrakar, Morrison, and Witte (2022). The CM1 governing equations of the Eulerian fields and the TAU bin scheme are integrated using 0.6 s time steps. The Lagrangian SDM scheme requires smaller substeps due to condensation/evaporation calculation with curvature and solute terms and the stochastic coalescence scheme (0.15 s for the current case). The SDM and TAU simulations are initialized with a uniform bi-modal lognormal distribution of ammonium sulfate aerosols from Ackerman et al. (2009) but with a factor of five reduced concentration (34 mg^{-1}) to accelerate the cellular transition process. The maximum radius of the initial (dry) aerosol distribution is set to 1 μm.

Various sensitivity tests are designed to investigate the impacts of aerosol scavenging and processing and to target the science questions posed in the introduction; these tests are listed in Tab. 1. In some of the tests using TAU, enhanced scavenging is considered by adding only a fraction of deactivated drops back to the aerosol population when

Table 1. Microphysical sensitivity tests presented in this article.

Case	Microphysics scheme	Aerosol input	Aerosol impaction scavenging
SDM	SDM	Aerosols from DYCOMS-II	Explicitly using a diffusion kernel
TAUSC90	TAU	Aerosols from DYCOMS-II	Implicit scavenging (replenish only 90% of deactivated drops to aerosols)
TAUSC80	TAU	Aerosols from DYCOMS-II	Implicit scavenging (replenish only 80% of deactivated drops to aerosols)
TAUSC70	TAU	Aerosols from DYCOMS-II	Implicit scavenging (replenish only 70% of deactivated drops to aerosols)
TAU-AERO-HI-PROC	TAU	Processed distribution shape from SDM but with the initial concentration	NO
TAU-AERO-LO-PROC	TAU	Processed distribution shape and number from SDM (mixing ratio: 16.5 mg^{-1})	NO
TAU-AERO-LO	TAU	Aerosol number from SDM (mixing ratio: 16.5 mg^{-1}) but with the initial distribution shape	NO

cloud and rain drops evaporate (which we refer to as "implicit" scavenging) to compensate for neglecting impaction scavenging. For example, in TAUSC90, TAUSC80, and TAUSC80, 90%, 80%, and 70% of deactivated drops are added back to the smallest unfilled aerosol bin relative to the initial background concentration, respectively. These sensitivity tests also help evaluate the impact of aerosol scavenging on cloud fields and precipitation evolution. The sensitivity test TAU-AERO-LO-PROC uses the processed aerosol distribution from SDM at 5 hours input into TAU at a simulation time of 3.5 hours. This test investigates the impact of the processed aerosol size distribution shape on the subsequent evolution of precipitation and the transition to open cells. TAU-AERO-HI-PROC is the same as TAU-AERO-LO-PROC except it scales the input processed aerosol distribution to give the same total aerosol concentration as at the beginning of the baseline TAU and SDM runs. TAU-AERO-LO also modifies the input aerosol at 3.5 hours and uses the same aerosol concentration as TAU-AERO-LO-PROC but with the initial aerosol distribution shape. Thus, comparing TAU-AERO-LO-PROC, TAU-AERO-HI-PROC, and TAU-AERO-LO helps to isolate the impact of reduced concentration via scavenging versus changes to the shape of the aerosol distribution via processing.

3 Results

3.1 Cloud field evolution in the SDM simulation with explicit aerosol physics

Figure 1(left) displays the cloud water path (CWP) and transient macroscopic cloud structure as the cloud system evolves with aerosol-cloud microphysical interactions in the SDM run. The cloud structure grows with time to larger organized closed cells with "cloud holes" at the edges. At 422 min of simulation time, CWP shows a clear break-

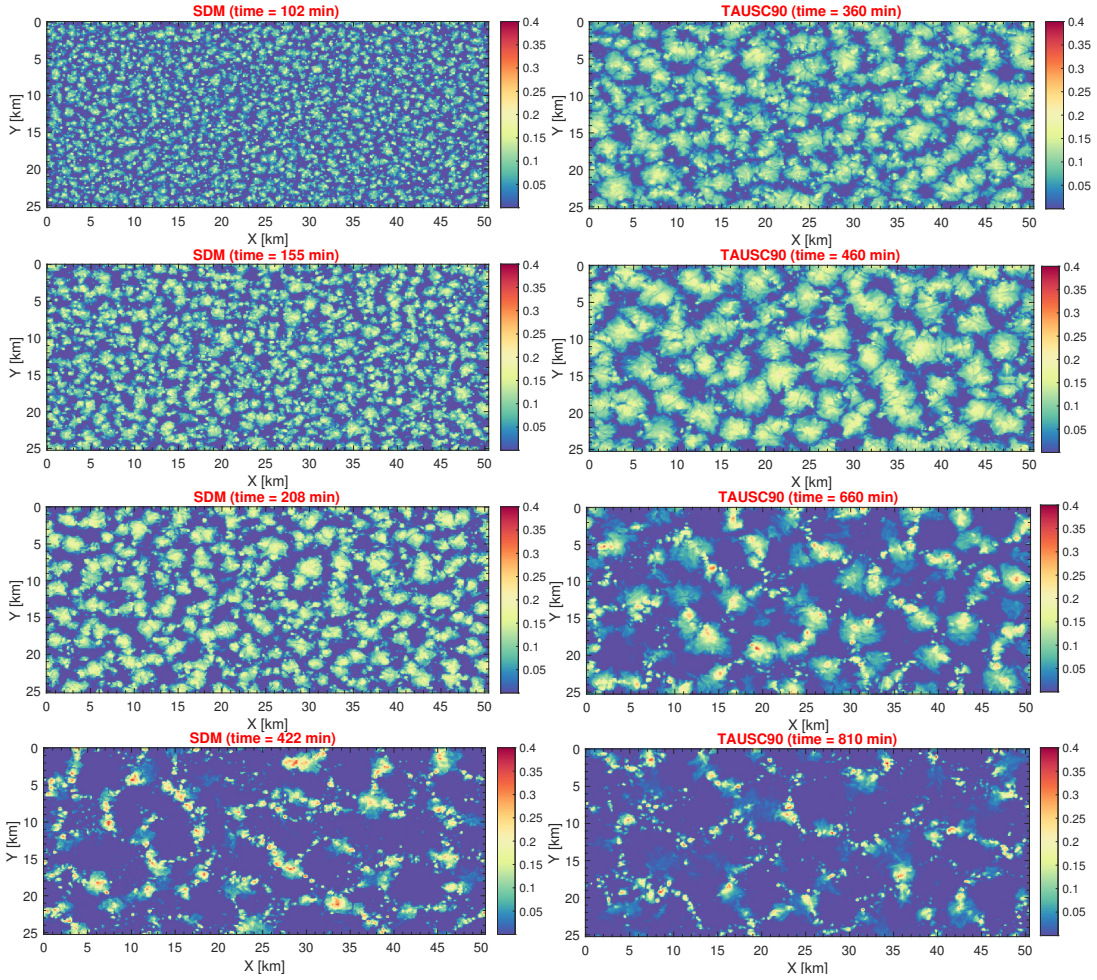

Figure 1. Comparison of cloud water path at different times during the cellular transition in SDM and TAUSC90 runs. The colorbars show magnitude in kg m^{-2}.

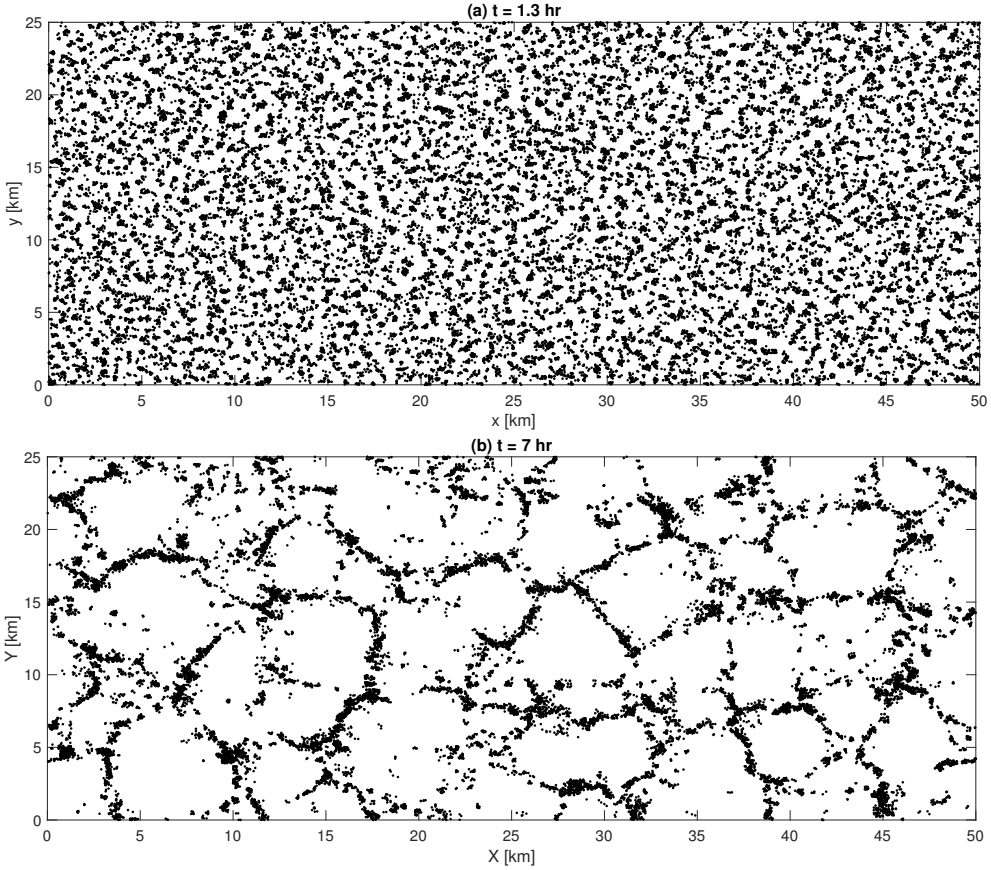

Figure 2. Cloud droplet activation locations in X-Y plane during (a) closed and (b) open cellular phase of the stratocumulus evolution from the SDM run. It is based on individual super-particle outputs from 30 sec of simulation time. The activation radius threshold based on the Köhler theory is used to determine activated super-particles.

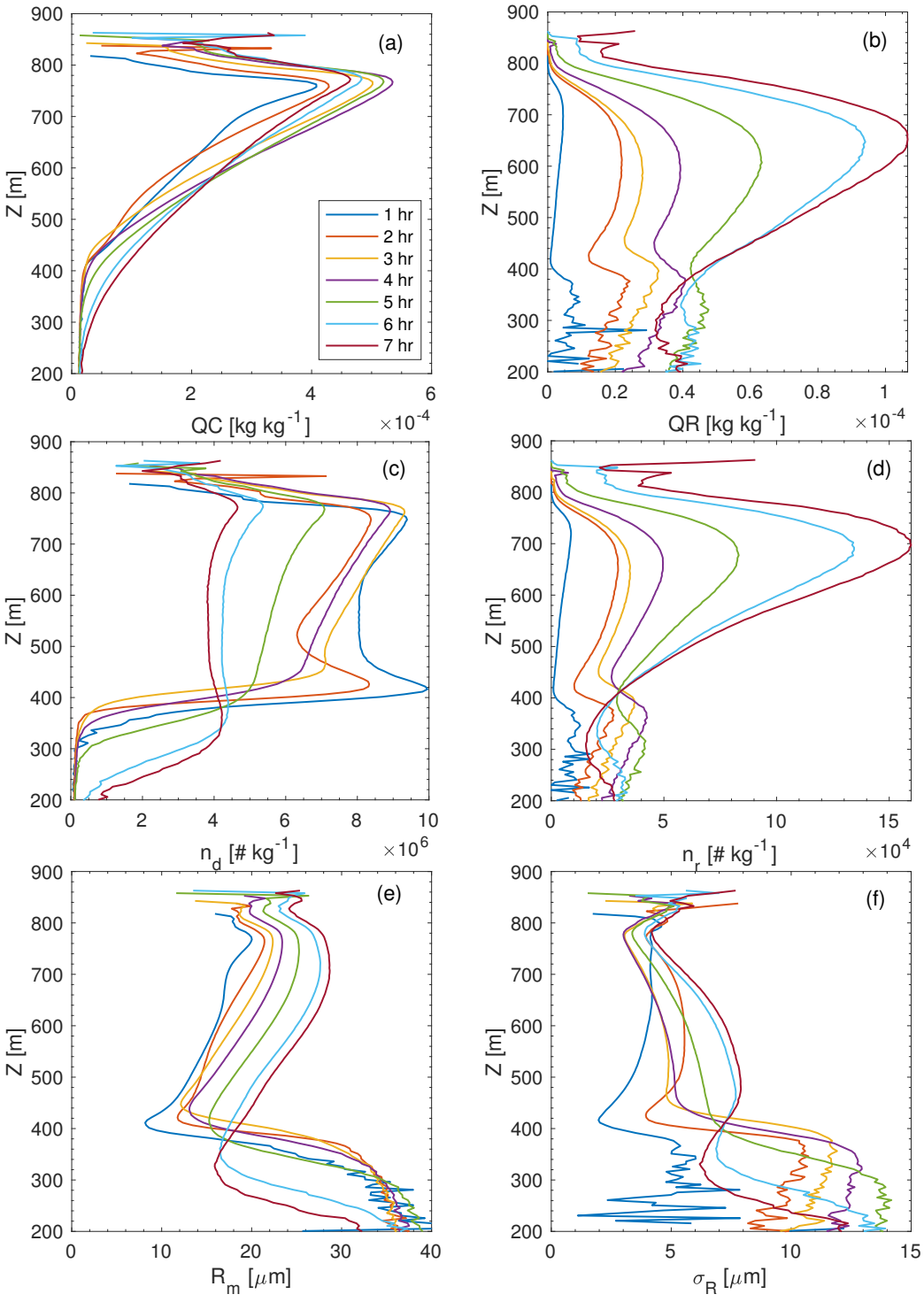

Figure 3. Average in-cloud vertical profiles of (a) cloud water mixing ratio (b) rain water mixing ratio (c) cloud droplet number mixing ratio (d) rain drop number mixing ratio (e) mean radius, and (d) radius standard deviation at different simulation times from the SDM run. These profiles are obtained from spatiotemporal averaging (3 samples within 15 min time windows) over cloudy grid cells ($qc > 10^{-5}$ kg kg^{-1}).

down from closed to open cell structures with large cloud water path in narrow updrafts at cell boundaries and wider cloud-free regions in downdrafts. Figure 2 illustrates the pattern of drop activation at two different simulation times with closed versus open cells from the SDM simulation, demonstrating distinctly different droplet activation variability associated with mesoscale cellular structures. During the initial closed cell phase, droplet activation occurs in small-scale updrafts scattered throughout the cloud field, and after transitioning to the open cell state, it mainly occurs in stronger cloud updrafts located near cell boundaries. For the same setup, Chandrakar, Morrison, and Witte (2022) showed that this cellular transition occurs when the drop coalescence time becomes shorter than the large eddy turnover timescale, leading to greater drop coalescence and increased precipitation flux. While the eddy turnover timescale is fairly steady, the coalescence timescale is linked to the mean drop radius and DSD width and evolves over time. This evolution of the DSD is closely tied to the aerosol concentration in the cloud system, driving droplet activation and controlling the phase relaxation timescale (a measure of the competition for the water vapor field). This suggests a critical role of aerosol removal (scavenging) in the transition process for a given meteorological condition and begs further investigation. The role of aerosol scavenging in the transition has been suggested in past studies as well (e.g., Mechem et al., 2006; Kazil et al., 2011; Berner et al., 2013; Erfani et al., 2022), but using models that did not explicitly represent cloud-borne aerosols and cloud processing and scavenging of aerosols.

Figure 3 shows changes in the mean vertical profiles of cloud properties (40 μm cloud-rain threshold radius) as the cloud field evolves. The peak cloud water mixing ratio increases with time up to four hours (4.08×10^{-4} to 5.35×10^{-4} kg kg^{-1}). Then it slightly decreases when transitioning to open cells. This trend of cloud water is opposite to the rain water evolution; the mean rain mixing ratio increases slowly (4.55×10^{-6} to 3.92×10^{-5} kg kg^{-1}) during the first four hours but increases at a faster rate thereafter (1.06×10^{-4} kg kg^{-1} at 7 hours). However, below $\sim$ 500 m, the mean cloud water mixing ratio has a larger magnitude during the open cellular phase (6-7 hours) than at earlier times (e.g., $\sim 5.67\times10^{-5}$ kg kg^{-1} increase between 4-7 hours at 400 m). This is likely from drizzle drops that evaporate to smaller sizes (crossing the 40 μm cloud-rain threshold radius) in downdrafts. This causes fluctuations in the cloud base height (and affects droplet activation as well, not shown), as evident by the droplet number concentration profiles. A sharp vertical gradient in cloud droplet number concentration near the cloud base becomes smoother over time, and in the open cellular phase, the drop concentration is higher below $\sim$ 370 m than in the closed cell phase (e.g., $\sim 3.6 \times 10^6$ kg^{-1} increase between 4-7 hours at 350 m). But overall, the droplet concentration decreases with time at all other altitudes due to aerosol scavenging, i.e., droplet loss from collision-coalescence and deactivation that overwhelms the activation flux. Could this also hint at cloud processing of aerosols that produce larger CCN after evaporation in the lower part of the boundary layer? We explore this possibility in detail in later subsections. Droplet concentration profiles in the upper part of the cloud layer show a peak near the cloud top, indicating activation of entrained aerosols. The rain drop concentration peaks around 700 m and decreases above due to transport/sedimentation, such that the height of the peak rain drop concentration is about 150 m below cloud top (see Fig. 1 in Chandrakar, Morrison, & Witte, 2022).

The mean cloud droplet radius R_m increases above 400 m, as expected for rising cloud parcels. Near cloud top, R_m decreases due to entrainment and evaporation as well as activation of new (small) droplets. Below 400 m, R_m is larger because of evaporating drizzle drops crossing the cloud-rain size threshold. The increase in mean radius with decreasing height is less sharp after transitioning to open cells (the difference in R_m between 200 and 410 m changes from $\sim$29 to 13 μm between 1 to 7 hours). This is due to differences in droplet activation, as discussed above.

Vertical profiles of the standard deviation of droplet radius within each grid cell σ_R, averaged over all cloudy points, exhibit some interesting features as the transition progresses. During the first two hours, σ_R increases with height by about 1.5-2.5 μm between ∼400 and 600 m (note it slightly decreases between ∼600 m to just below cloud top at 2 hours). This increase of σ_R with altitude is from the mixing of cloud parcels with different growth histories in closed cell updrafts as well as some mixing at the updraft-downdraft interface (Chandrakar, Morrison, & Witte, 2022). A sharper increase of σ_R near cloud top ($\Delta\sigma_R \sim 0.5$, 2, and 1.7 μm at t = 1, 4, and 7 hours, respectively) is from entertainment-mixing and associated drop activation that changes with time due to the change in turbulence intensity and boundary layer aerosol concentration. Interestingly, profiles after 2 hours show a decrease of σ_R with altitude above 450 m (decrease between 450 and 800 m of ∼1.8 μm at 3 hours and 3.7 μm at 7 hours), although the magnitude of the average σ_R increases with time after 4 hours. The rate of decrease with altitude also increases with time. More evaporation of drizzle drops in downdrafts, their mixing with updraft regions, and higher variability in drop age due to the overturning motion of large eddies lead to a larger DSD width at lower altitudes at later times when there is more drizzle in clouds (Chandrakar, Morrison, & Witte, 2022). The magnitude of the mean σ_R increases with time due to greater supersaturation variability as the cloud gets cleaner and as drop collision-coalescence increases. Mean σ_R below 400 m also increases sharply with decreasing altitude (difference in σ_R between 200 and 400 m increasing from ∼4–7.6 μm between 1 and 5 hr) because of evaporating drizzle drops. After the transition to open cells, activation of new droplets between 200 and 400 m dominates the distribution and reduces the magnitude of σ_R.

3.2 Role of aerosol scavenging on the transition to open cells

When a stratocumulus system evolves with time, it progressively gets cleaner without significant external aerosol sources. The wet scavenging of aerosols through cloud formation and coalescence causes the concentrations of both cloud droplets and aerosols to decrease with time. The coalescence of cloud and drizzle drops and diffusion of aerosols to drops increase the solute mass of aerosols in drops. Once they evaporate in the lower part of the boundary layer, they are available again for cloud formation but with a greater potential for activation and growth due to their larger sizes. Figure 4 demonstrates this physical aerosol processing by clouds and resultant dry aerosol distribution after sufficient cloud cycling (time = 7 hours) at different altitudes. At all altitudes, the right tail of dry aerosol distributions is broader than the initial background aerosol distribution. This enhanced concentration of large aerosols and larger maximum sizes than the original aerosol distribution (2.5 μm versus 1 μm) suggests significant processing of aerosols. With a decrease in altitude, the relative concentration of large aerosol particles in the distribution tail and maximum particle size increase. At 200-250 m, an additional large aerosol mode with modal radius of about 300 nm is apparent. This large aerosol mode at lower levels is explained by the higher fall speeds of large drizzle drops, which are more likely to contain large solute mass compared to smaller cloud drops. These faster-falling drizzle drops are able to survive well below cloud base prior to evaporating, thereby regenerating large aerosol particles at low levels.

Figure 5 shows the decay of in-cloud and boundary layer averaged aerosol concentrations in the SDM and TAU runs listed in Tab. 1. A sharp reduction of in-cloud aerosols (Fig. 5a) within the first hour (∼ 45% in 30 min) in all of the TAU runs suggests a higher activation rate, but this is balanced by a higher deactivation rate to give a similar decay rate of boundary layer-averaged aerosol concentration as SDM (Fig. 5b). After the first hour, aerosol concentration is depleted significantly faster in SDM compared to TAUSC90 and TAUSC80 (e-folding timescale ∼ 8.3 and 6.9 hours, respectively, versus 5.6 hours for SDM in the cloud layer) in both the cloud layer and through the entire boundary layer. A faster decay rate in SDM is due to impaction scavenging of aerosols by cloud and drizzle drops (neglected in TAU) and faster removal through precipitation. Larger differences

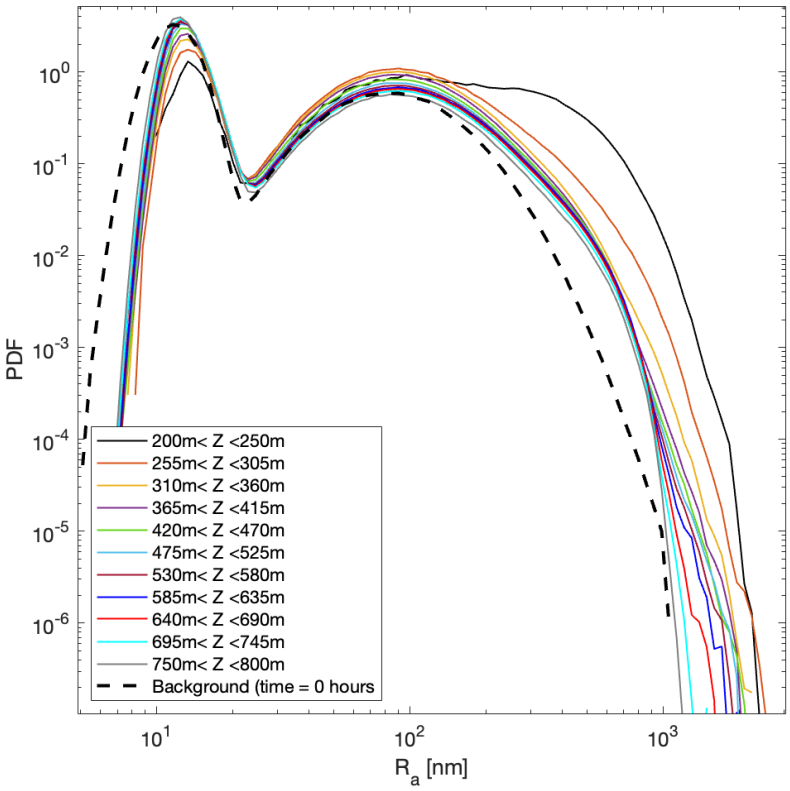

Figure 4. Distributions of solute radius in activated droplets (solid lines) at different altitudes from t = 7 hours from the SDM run and their comparison with the initial aerosol distribution (black dashed-line).

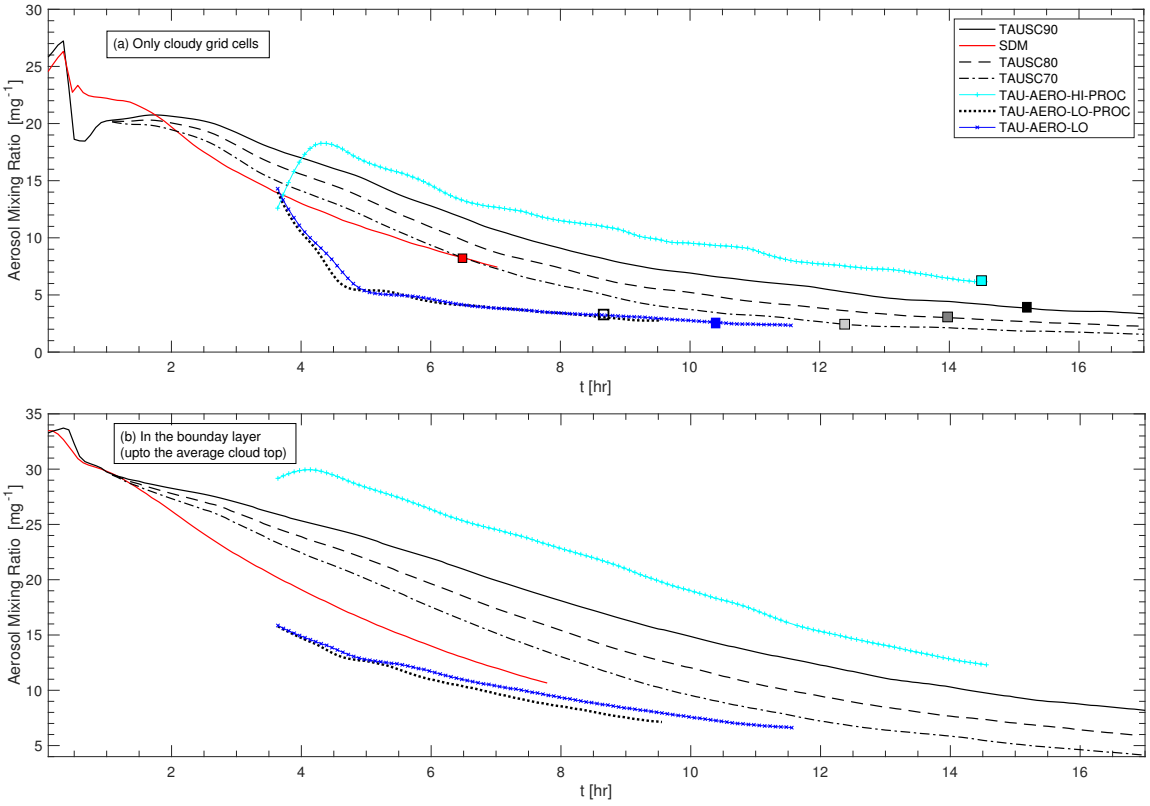

Figure 5. Time series of aerosol mixing ratio averaged over (a) cloudy grid cells ($qc > 10^{-5}$ kg kg^{-1}) and (b) the entire boundary layer up to the average cloud top. Different lines are from the SDM and TAU runs listed in Table 1. Squares mark the transition time to open cells.

in average boundary layer aerosol concentration between SDM and TAU begin around the time when surface precipitation deviates significantly between the simulations (discussed in the following subsection).

As shown in Fig. 5, the implicit scavenging in TAUSC90 and TAUSC80 is insufficient to match the in-cloud aerosol decay in the SDM run. With an increase in implicit scavenging compared to TAUSC90 and TAUSC80, the TAUSC70 run is similar to the SDM aerosol decay rate within the cloud layer ($\sim$ 5.9 hours e-folding timescale for TAUSC70). However, TAUSC70 still produces insufficient depletion of average boundary layer aerosol concentration, with a mean aerosol number mixing ratio about 3-4 mg^{-1} higher in TAUSC70 than SDM (e-folding timescale 8.1 hours versus 6.6 hours). Reduced loss of boundary layer aerosol suggests that the precipitation loss is lower for TAU runs; that is, there is less drizzle formation and more evaporation in the boundary layer. It is important to note that aerosol processing is not considered in any of these TAU runs (TAUSC90, TAUSC80, TAUSC70) while it is considered in SDM. This also impacts how aerosols participate in cloud cycling and, thus, affects the aerosol removal in a positive feedback loop.

The impact of aerosol processing is further investigated by using TAU but with a processed aerosol distribution from SDM (at 5 hours, about 1.5 hours before the transition to open cells in SDM). The processed aerosol distribution is included in TAU at a simulation time of 3.5 hours (TAU-AERO-LO-PROC), and the aerosol concentration thereafter is rapidly depleted (a factor $\sim$ 1.5 decrease of the in-cloud aerosol concentration within an hour) as aerosols activate as cloud droplets. This rapid depletion through droplet activation in TAU could be due to the quasi-equilibrium assumption and neglect of growth kinetics during the activation process (Chuang et al., 1997). A greater activation loss of aerosols in TAU compared to SDM is also consistent with larger droplet activation rates near cloud base in cumulus congestus simulations (Chandrakar, Morrison, Grabowski, & Bryan, 2022). After this initial adjustment, the aerosol concentration is significantly lower in TAU-AERO-LO-PROC. However, the decrease in aerosol concentration is much slower in the cloud layer after this initial adjustment since no additional impaction scavenging exists. To contrast the impact of this clean and processed aerosol environment, we performed two additional sensitivity simulations (restarting from the same time at 3.5 hours): (a) TAU-AERO-LO, with the same reduced aerosol concentration as TAU-AERO-LO-PROC but with the initial (unprocessed) aerosol distribution shape; and (b) TAU-AERO-HI-PROC, with the processed distribution shape from SDM but with the initial aerosol concentration. For TAU-AERO-LO, in-cloud aerosols decrease at a similar rate as TAU-AERO-LO-PROC during the rapid adjustment period from 3.5 to 4.5 hours. However, the loss of aerosol in the boundary layer in TAU-AERO-LO is somewhat slower than TAU-AERO-LO-PROC, consistent with an enhanced precipitation-induced loss when the processed aerosol distribution shape is used in TAU-AERO-LO-PROC. Since TAU-AERO-HI-PROC is restarted at 3.5 hours with the initial aerosol concentration, it has a significantly higher aerosol concentration than in all other runs. TAU-AERO-HI-PROC shows a similar rate of decrease in both cloud layer and boundary layer aerosol concentration as TAUSC90, even without any implicit scavenging in TAU-AERO-HI-PROC. This implies that the processed aerosol distribution shape leads to enhanced scavenging in TAU-AERO-HI-PROC, which compensates for the lack of implicit scavenging.

Impacts of aerosol scavenging and processing on the transition to open cells are demonstrated in Fig. 1. Cloud water path for the SDM run, which includes both physical processing of aerosols and impaction scavenging, evolves to an open cell structure significantly faster than TAUSC90 (in about one-half of the simulation time) and the other TAU runs. The sizes of the closed cells are also larger in the TAU runs than in SDM. Squares in Fig. 5a also mark the transition point from closed to open cells (defined by cloud fraction $<\approx 56\%$) for all runs. These results show that increased implicit scavenging in TAU (from TAUSC90 to TAUSC80 and TAUSC70) leads to a systematic decrease

in the time of transition to open cells. Similarly, reduced aerosol concentration in TAU-AERO-LO compared to the other TAU simulations leads to a faster transition. With the processed aerosol distribution input at 3.5 hours in TAU-AERO-LO-PROC, the transition happens earlier than in TAU-AERO-LO by nearly 2 hours. Moreover, the transition is about 45 min faster with the processed aerosol distribution in TAU-AERO-HI-PROC than TAUSC90 despite the lower in-cloud and boundary layer aerosol concentrations and the presence of implicit scavenging in the latter. Overall, these results indicate that both the loss of aerosol concentration from scavenging as well as the change in aerosol size distribution shape from aerosol processing are important in determining the timing of the transition to open cells.

3.3 Comparison of cloud, precipitation, and dynamics evolution in Lagrangian SDM and Eulerian TAU bin simulations

Figure 6 compares the average properties of cloud and rain (cloud and rain water mass and number mixing ratios, mean drop radius, and spectral width), vertically integrated quantities (cloud fraction and liquid water path), dynamics (TKE and vertical velocity skewness), and the surface precipitation rate. The mean and standard deviation of the drop radius are based on drop size distributions in each grid cell. The cloud and rain statistics are averaged over all cloudy grid cells ($qc > 10^{-5}$ kg kg^{-1}). The peak cloud water mixing ratio (2.8×10^{-4} kg kg^{-1}) is the second largest for SDM (after 2.9×10^{-4} kg kg^{-1} for TAU-AERO-HI-PROC), and it reaches a peak magnitude earlier than all TAU runs (4 versus 8 hours). A lower magnitude of cloud water in most TAU runs is consistent with greater evaporation from numerical diffusion along cloud boundaries (compared to the Lagrangian treatment in SDM), similar to differences between TAU and SDM in cumulus congestus simulations (e.g., Chandrakar, Morrison, Grabowski, & Bryan, 2022). The rain water mixing ratio also increases significantly faster to a larger magnitude in SDM (8.25×10^{-5} kg kg^{-1} at 7.45 hours) than in all TAU runs (e.g., 7.42×10^{-5} kg kg^{-1} at 13.08 hours for TAUSC70). The rain water mixing ratio also increases faster with an increase in the implicit scavenging rate in TAU (from TAUSC90 to TAUSC80 and TAUSC70). Changes in rain water mixing ratio are generally consistent with changes in cloud mixing ratio, with faster increases in rain mixing ratio associated with decreases in cloud mixing ratio. For example, cloud water mixing ratio decreases faster after ~ 7 hours with an increase in the implicit scavenging for TAU. With the processed aerosol distribution input into TAU-AERO-LO-PROC at 3.5 hours, rain water mixing ratio increases faster than in TAU-AERO-LO with its unprocessed aerosol distribution. Thus, both increased scavenging as well as aerosol processing increase the formation of rain using TAU. After initial adjustment, the cloud water evolution for TAU-AERO-LO-PROC nearly matches SDM. The rate of rain water increase over time is also similar between SDM and TAU-AERO-LO-PROC. The cloud droplet number mixing ratio is similar between the SDM and TAU runs before ~ 3 hours, but the rain drop number mixing ratio is higher in SDM. After 3 hours, differences in the cloud and rain drop number mixing ratios among the simulations are similar to the mass mixing ratios.

The mean drop size increases over time faster in SDM than all of the TAU runs, which is consistent with the cloud water mixing ratio plot. A larger mean radius in SDM (for a similar drop number concentration during the first three hours) is also consistent with spurious evaporation in the bin scheme from numerical diffusion of liquid water in physical space. The numerical representation of the Eulerian advection of the bin variables in the physical space might cause a spurious spread of cloud water to sub-saturated downdrafts and cloud holes, leading to the evaporation of cloud droplets. This numerical artifact seems to produce more homogeneous mixing-like behavior in TAU, i.e., liquid mass loss with a nearly similar number relative to SDM. Due to the Lagrangian framework, such numerical artifacts are absent in SDM. Reduction of cloud water with a similar droplet number as SDM (and thus smaller mean radius) also occurred in the upper part of the simulated cumulus congestus cloud using the TAU bin scheme in (Chandrakar,

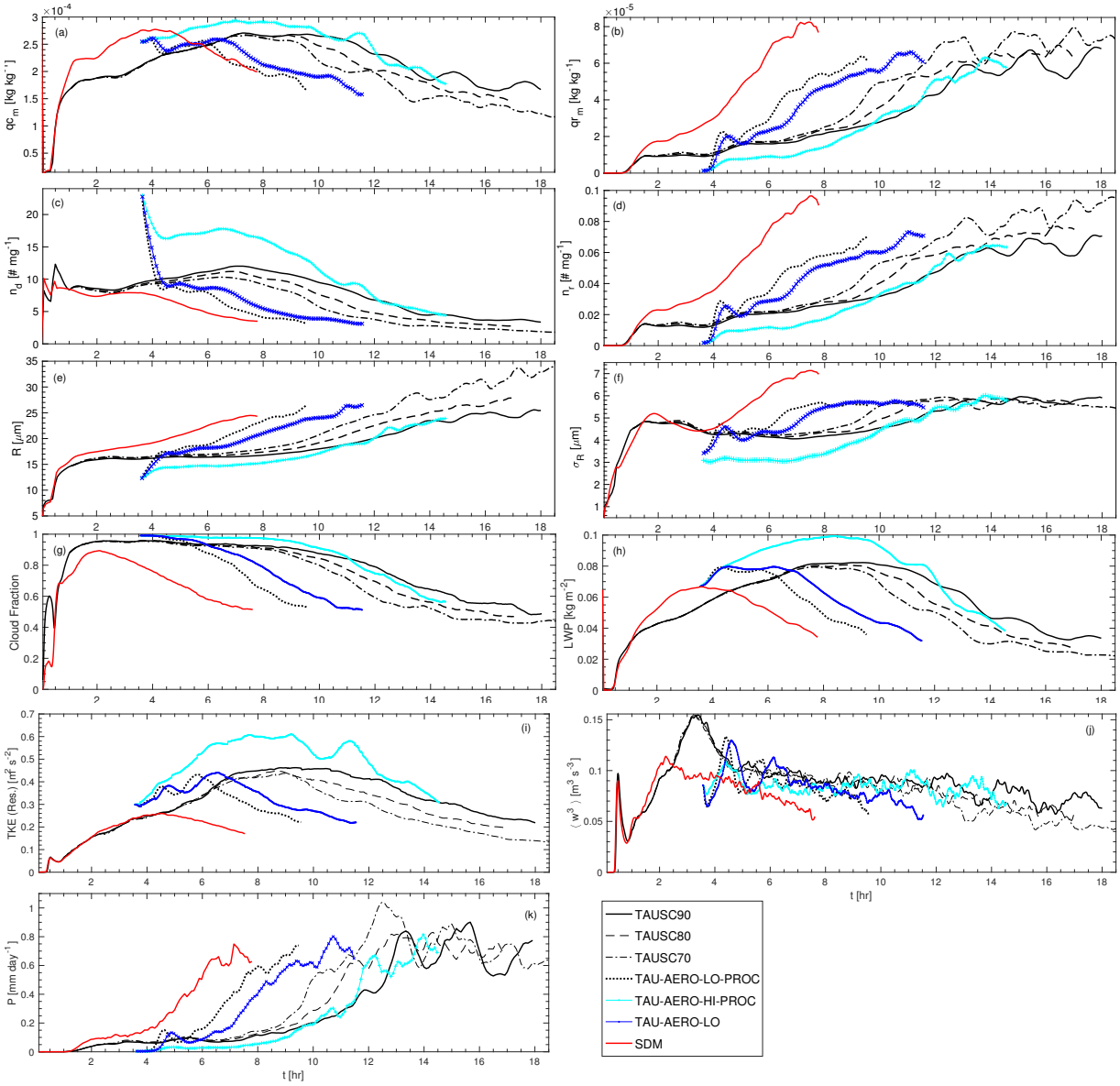

Figure 6. Time evolution of average in-cloud statistics ($qc > 10^{-5}$ kg kg^{-1}) from the SDM and TAU runs listed in Table 1: (a) cloud water mixing ratio, (b) rain water mixing ratio, (c) cloud droplet number mixing ratio, (d) rain droplet number mixing ratio, (e) mean droplet radius, (f) standard deviation of droplet radius, (g) cloud fraction, and (h) liquid water path. Also shown are mean turbulence statistics in the cloud layer: (i) resolved turbulent kinetic energy and (j) vertical velocity skewness, and the (k) domain-mean surface precipitation rate.

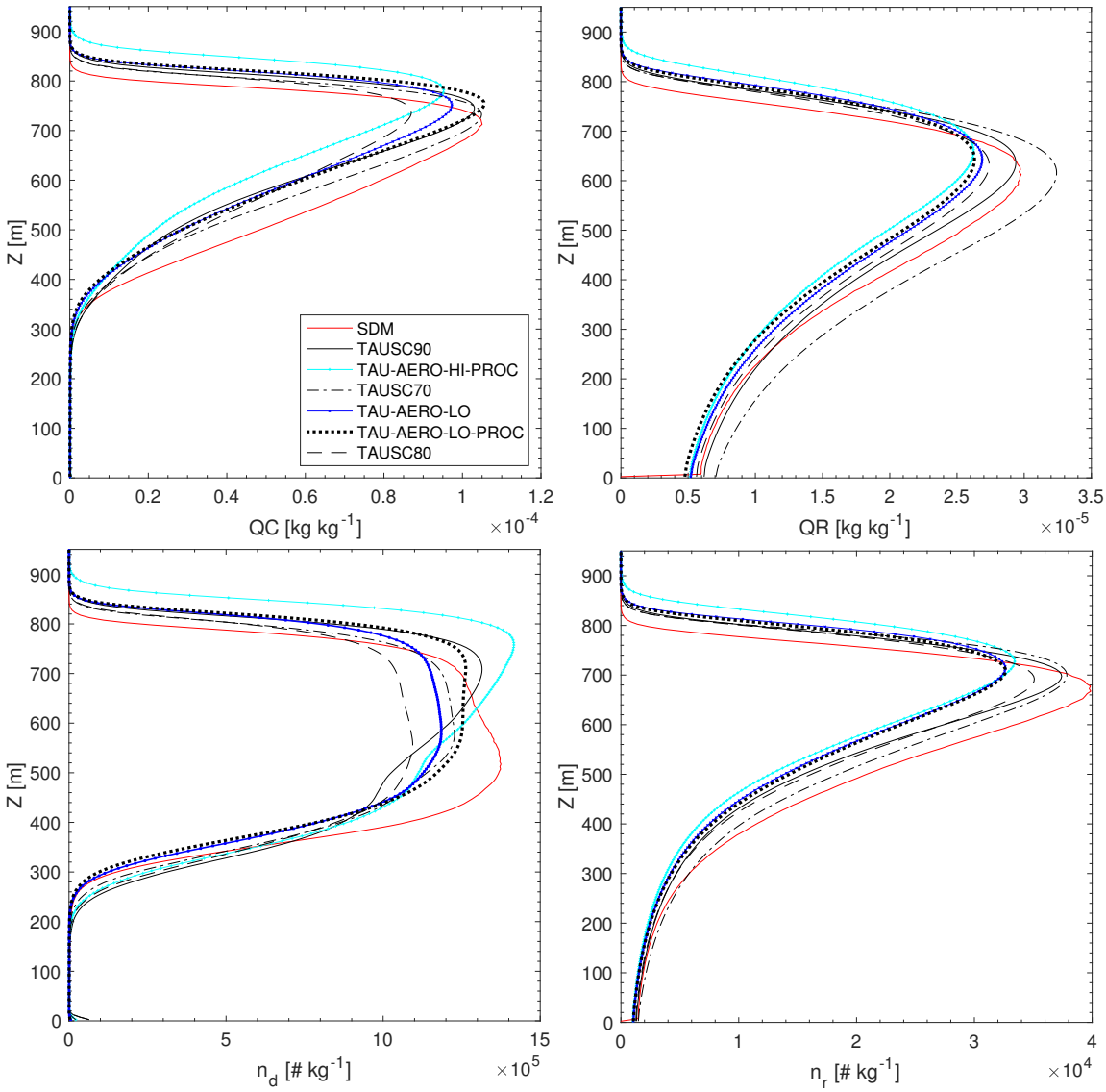

Figure 7. Domain-averaged vertical profiles of (a) cloud water, (b) rain water, (c) cloud droplet number, and (d) rain drop number mixing ratios from SDM and TAU runs during the open cellular phase (approximately the same cloud fraction 56%). Note that the simulation time used for the comparison varies since the transition time differs among the runs.

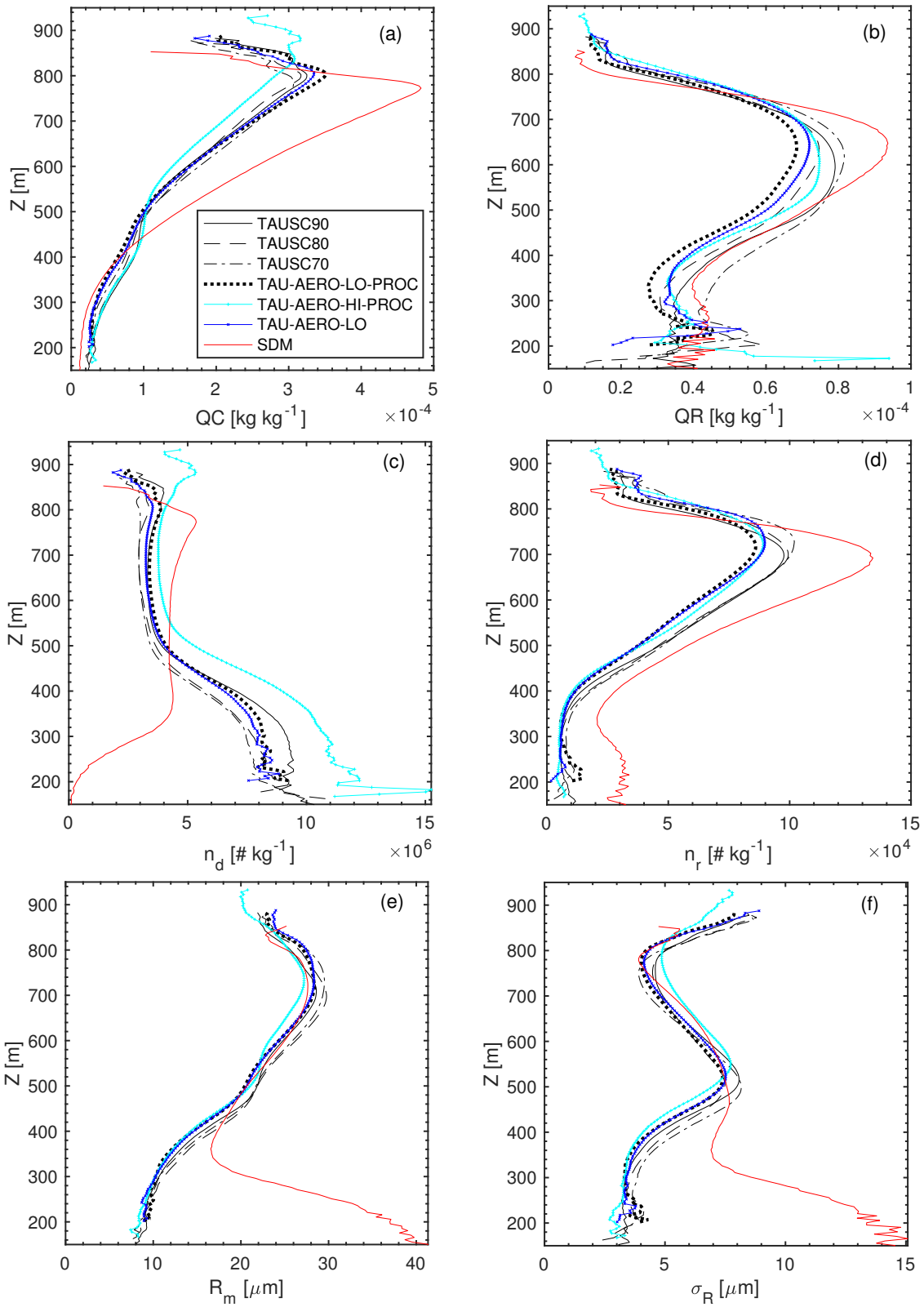

Figure 8. Comparison of in-cloud average ($qc > 10^{-5}$ kg kg^{-1}) vertical profiles of (a) cloud water, (b) rain water, (c) cloud droplet number, (d) rain drop number mixing ratios, (e) mean droplet radius, and (f) standard deviation of droplet radius from the SDM and TAU runs during the open cellular phase (same as Fig. 7 except in-cloud versus domain-averaged quantities).

Morrison, Grabowski, & Bryan, 2022). A larger mean drop radius is likely the trigger for faster development of rain within the first 3 hours in SDM. A positive feedback through aerosol scavenging and processing (i.e., more aerosol scavenging with processing due to faster rain growth that, in turn, enhances the acceleration of rain formation) is responsible for further enhancement of rain growth and aerosol removal in SDM, and consequently, changes in cloud droplet number and mean size. Thus, this three-component feedback, coupling cloud, rain, and aerosols, initially triggered by a larger mean cloud radius in SDM than TAU (due to the numerical diffusion in physical space in TAU), drives a faster transition to open cells in the SDM run. As discussed earlier, TAU does not explicitly consider aerosol processing and recirculation of the processed aerosols into clouds, which contributes to slower rain formation and transition to open cells. A faster increase of the mean drop size in TAU-AERO-LO-PROC compared to TAU-AERO-LO is shown in Fig. 6, providing clear evidence of the impact of the processed aerosol size distribution. The mean drop size response for different implicit scavenging rates in (TAUSC90, TAUSC80, TAUSC70) is consistent with the droplet mixing ratio differences.

The standard deviation of drop radius is similar between the SDM and TAU runs up to three hours of simulation time. After $\sim$ 3.5 hours, the radius standard deviation is significantly higher for SDM than all TAU runs ($\sim$7.14 versus 5.68 μm). Interestingly, this result contrasts with previous findings of broader droplet spectra using bin microphysics (relative to SDM) in simulations of cumulus congestus clouds (Chandrakar, Morrison, Grabowski, & Bryan, 2022). A larger spectral width in cumulus congestus simulations is caused by significant numerical diffusion in droplet size space arising from vertical transport in the strong updraft environment with 50-100 m vertical grid spacing. However, offline tests in Morrison et al. (2018) showed that the vertical grid spacing is a key factor in numerical broadening of DSDs, and the vertical grid spacing is a factor of ten smaller in the current stratocumulus case (5 m). Thus, the numerical broadening in the current stratocumulus TAU runs appears to have less impact than in the congestus case of Chandrakar, Morrison, Grabowski, and Bryan (2022). A smaller spectral width in TAU runs than SDM is also likely from reduced collision-coalescence and rain formation, as shown by the rain drop number and mass ratio time series. Similar to the mean drop radius, the mean radius standard deviation in the TAU runs also has a faster rate of increase after five hours with an increase in implicit scavenging. The mean radius standard deviation also responds similarly to the mean radius when the processed aerosol distribution from SDM is input into TAU (TAU-AERO-LO-PROC and TAU-AERO-HI-PROC). However, interestingly, over time the mean radius standard deviation in all of the TAU runs saturates to approximately the same value ($\sim$5.5 μm) after the transition from closed to open cells.

The integral cloud properties like cloud fraction and liquid water path follow time evolution consistent with the cloud water mixing ratio for each case. However, the cloud fraction is the lowest for SDM but it has a higher mean cloud water mixing ratio than the TAU runs, which is again consistent with numerical diffusion in TAU. The mean liquid water path (LWP) also increases faster over time in the SDM run, following the pattern of the mean cloud water mixing ratio.

Dynamical quantities also show a wide range of diversity among the simulations. The mean turbulent kinetic energy (TKE) follows the LWP response. Mean TKE values from the SDM and TAU simulations are similar prior to $\sim$ 4.5 hours, but it decreases thereafter in SDM with the reduced LWP and increased precipitation. The mean vertical velocity skewness in the cloud layer increases (i.e., updrafts get stronger) up to $\sim$ 2 hours and then decreases for SDM. However, for TAU runs, the vertical velocity skewness peak occurs later ($\sim$ 3.3 hours), likely due to the delay in rain formation affecting the sedimentation flux and, consequently, the stability of the cloud layer. The surface precipitation rate, a key quantity for the cellular transition process and aerosol removal (Stevens et al., 2005; Savic-Jovcic & Stevens, 2008; Wood et al., 2008; Goren & Rosen-

feld, 2012), also increases significantly faster in SDM than the TAU runs consistent with the other quantities discussed above. In SDM, the mean precipitation rate sharply increases beginning at ∼4 hours, coincident with the decrease in cloud water mixing ratio, liquid water path, and TKE. For TAU runs, the surface precipitation rate increases earlier as the implicit aerosol scavenging is increased, but surface precipitation is substantially delayed relative to SDM in all cases. When the aerosol distribution from SDM is used in TAU (TAU-AERO-LO-PROC), the rate of increase in precipitation is similar to SDM although delayed about 1.5 hours owing to spinup since the processed aerosol is not input in TAU-AERO-LO-PROC until 3.5 hours. Moreover, the increase in precipitation is delayed ∼45 min in TAU-AERO-LO compared to TAU-AERO-LO-PROC. This illustrates the impact of changes in aerosol size distribution shape from aerosol processing since both runs input the same reduced aerosol concentration from SDM.

Figure 7 compares the domain-averaged vertical profiles (without any threshold for cloud water) of cloud and rain water number and mass mixing ratios after the transition to open cells. These profiles are similar between the SDM and TAU runs. However, the cloud top is slightly lower, and the cloud water mixing ratio is slightly larger for SDM compared to all TAU runs between 350-700 m. When comparing the average profiles of cloud and rain quantities based on a threshold for cloudy grid cells $qc > 10^{-5}$ kg kg^{-1} (Fig. 8), differences between SDM and TAU runs are more evident. Between 450-800 m, SDM has a significantly higher mean cloud water mixing ratio (SDM versus TAU peaks: 4.8×10^{-4} kg kg^{-1} versus 3.5×10^{-4} kg kg^{-1}). This suggests the cloud field is more diffused in TAU even after the transition to open cells, again likely from the numerical diffusion. The in-cloud rain water peak is also slightly stronger in SDM ($9.3{\times}10^{-5}$ kg kg^{-1}) than in TAU (max $\sim 8.1{\times}10^{-5}$ kg kg^{-1}), and the rain drop number mixing ratio is larger in SDM (peak: $1.3{\times}10^{5}$ kg^{-1}) than TAU (peak max $\sim 1.0{\times}10^{5}$ kg^{-1}) at all levels below 750 m. A smaller drop number but similar rain water below the peak rainwater implies that the mean rain drop size is slightly larger in TAU runs. The cloud droplet number mixing ratio profiles (averaged over cloudy grid cells) differ drastically between SDM and TAU runs. SDM has a nearly uniform number mixing ratio in the cloud layer that sharply decreases near the top. Similarly, below 350 m, it gradually drops to zero. However, for the TAU runs, there is a nearly uniform number mixing ratio above 500 m, but it increases below this level to a significantly larger value than in SDM. This result suggests more activation of cloud droplets at lower levels from moistening of the boundary layer in TAU. A more diffuse liquid water field in the Eulerian TAU simulations could explain boundary layer moistening via increased evaporation in downdrafts. Moreover, as discussed earlier, the quasi-equilibrium assumption and the neglect of growth kinetics during the activation process (Chuang et al., 1997) may also cause a higher droplet activation rate in TAU. The presence of a large concentration of in-cloud drizzle drops (likely near the cloud-drizzle threshold) and small cloud droplet concentration in SDM causes the mean and standard deviation of drop radius to deviate from TAU runs below 450 m (a larger mean and standard deviation in SDM). Otherwise, they are nearly the same for SDM and TAU runs above 450 m.

4 Summary and Conclusions

Shallow boundary layer clouds are a critical component of global climate and are sensitive to anthropogenic pollution. Complex interactions between aerosol, cloud, and precipitation at various scales make these clouds interesting but also challenging to represent in climate models. Even process-level models struggle to represent aerosol-cloud-precipitation interactions explicitly due complications from cloud-borne aerosol and aerosol processing. Lagrangian particle-based microphysics schemes are particularly well-suited to account for these interactions with fewer simplifications and assumptions compared to traditional Eulerian schemes. We utilized this tool (the Super-Droplet Method, or SDM) to investigate the evolution of cloud micro- and macro-physical properties and physical

aerosol scavenging and processing during the mesoscale transition to open cells, extending the analysis presented in Chandrakar, Morrison, and Witte (2022). By contrasting results from SDM with simulations using the TAU bin scheme, we determined the impact of aerosol scavenging and processing on precipitation generation and the transition process. The impacts of simplifying aerosol-cloud interactions and numerical diffusion in the Eulerian bin scheme (TAU) on cloud field evolution, the mesoscale transition, and cloud properties in the final open-cell state were further investigated by comparing SDM and TAU results.

The simulation using Lagrangian microphysics with explicit aerosol activation and impaction scavenging showed significant physical processing of aerosols that impacted precipitation generation and evolution of the cloud field. Both changes in aerosol distribution shape from processing and reduced concentration from scavenging were shown to be important for the aerosol removal rate through precipitation. Past observations (e.g., Sharon et al., 2006) indicated that the presence of extremely clean conditions coincides with the cellular regions. In this study, we showed that physical processing of aerosol and changes in aerosol size distribution shape also impact the time for transition to open cells; an earlier transition occurred due to the processed aerosol distribution shape.

This study provided detailed insights into the evolution of the vertical structure of cloud and rain quantities during the closed-to-open-cell transition. During the open cell stage, moistening of the boundary layer caused droplet activation to occur at lower levels than the initial cloud base, resulting in a smaller DSD mean and standard deviation at lower levels using SDM. Although the DSD mean and standard deviation increased overall, DSD width had a progressively steeper decreasing profile with height during the transition to open cells, contrasting with an increasing profile during the earlier closed cell phase. This was explained by more drizzle formation, the evaporation of drizzle drops in downdrafts, and mixing of drops of different growth history producing broader DSDs at lower compared to upper levels after the transition to open cells.

The simulation with SDM was compared to TAU simulations that applied an implicit representation of aerosol scavenging without aerosol processing. The TAU runs had a significant delay in the transition to open cells compared to SDM, even when the implicit aerosol scavenging was increased to match the in-cloud aerosol concentration evolution in SDM. TAU runs could not capture the rapid decay of boundary layer aerosol concentration that occurred with SDM. Sensitivity tests suggested that the representation of aerosol processing is important for removing aerosols through precipitation. Spurious evaporation in TAU from numerical diffusion along cloud boundaries also reduced cloud water and mean droplet size compared to SDM. A larger mean drop radius and greater cloud water mixing ratios helped to initiate faster rain development in SDM. After the initial phase, a positive feedback associated with enhanced aerosol scavenging due to faster rain growth in turn further enhanced rain formation in SDM. This feedback was responsible for accelerated aerosol removal and, consequently, reduced cloud droplet number, increased mean droplet size, and increased spectral width. Thus, a positive feedback via aerosol-cloud-precipitation interactions combined with initially larger mean radius and cloud water mixing ratios helped to drive a faster transition to open cells in SDM compared to TAU.

The absence of aerosol processing and recirculation of the processed aerosols into clouds in TAU was another key factor for slower rain formation and transition to open cells. Interestingly, this result contrasts with previous findings of broader droplet spectra using bin microphysics (relative to SDM), which led to faster precipitation generation in simulations of cumulus congestus clouds (Chandrakar, Morrison, Grabowski, & Bryan, 2022). This suggests that aerosol-cloud-precipitation interactions in SDM dominated the effects of numerical broadening in TAU for this stratocumulus case (a much smaller vertical grid spacing, which impacts the degree of numerical DSD broadening, in the current study compared to the earlier cumulus congestus simulations may have

also contributed to a reduced impact of numerical DSD broadening here). After the transition to open cells, some differences in cloud and rain quantities between SDM and TAU persisted. More droplet activation below 400 m in TAU runs caused a deviation in the mean and standard deviation of drop radius compared to SDM.

This study highlights the importance of aerosol scavenging and physical aerosol processing on drizzle formation and the open cell transition using a state-of-the-art modeling tool (LES with a super-particle microphysics scheme) with an explicit, detailed representation of aerosol-cloud interactions. Recent advances in computing power have made LES with Lagrangian particle-based microphysics feasible over a mesoscale domain. This work built upon previous studies on aerosol processing and the mesoscale transition using models with simpler microphysics schemes (e.g., Feingold & Kreidenweis, 2002; Kazil et al., 2011; Goren et al., 2019; Erfani et al., 2022). Further studies on several related topics, including detailed quantification of aerosol scavenging and processing in different cloud regions, statistics of the recycling of processed aerosols, impacts of initially clean versus polluted aerosol conditions, and the role of chemical aerosol processing, are possible using LES with the Lagrangian super-particle scheme. This would further improve understanding of aerosol-cloud interactions in stratocumulus clouds and help to inform bulk microphysics parameterizations.

Open Research

The current study used the CM1 model release 19.8 for the simulations presented here. CM1 code with detail documentation and DYCOMS-II RF02 case setup is available at `https://www2.mmm.ucar.edu/people/bryan/cm1/`. SDM code provided by Shinichiro Shima is available at `https://github.com/Shima-Lab/SCALE-SDM_BOMEX_Sato2018`.

Acknowledgments

This material is based upon work supported by the NSF National Center for Atmospheric Research, which is a major facility sponsored by the National Science Foundation under Cooperative Agreement No. 1852977. It was also supported in part by U.S. Department of Energy grants DE-SC0020118 and DE-SC0023151. We would like to acknowledge high-performance computing support from Cheyenne (doi:10.5065/D6RX99HX) provided by NCAR's Computational and Information Systems Laboratory, sponsored by the NSF National Science Foundation.

References

Ackerman, A. S., Kirkpatrick, M. P., Stevens, D. E., & Toon, O. B. (2004). The impact of humidity above stratiform clouds on indirect aerosol climate forcing. *Nature*, *432*(7020), 1014–1017.

Ackerman, A. S., VanZanten, M. C., Stevens, B., Savic-Jovcic, V., Bretherton, C. S., Chlond, A., ... others (2009). Large-eddy simulations of a drizzling, stratocumulus-topped marine boundary layer. *Monthly Weather Review*, *137*(3), 1083–1110.

Albrecht, B. A. (1989). Aerosols, cloud microphysics, and fractional cloudiness. *Science*, *245*(4923), 1227–1230.

Andrejczuk, M., Grabowski, W., Reisner, J., & Gadian, A. (2010). Cloud-aerosol interactions for boundary layer stratocumulus in the lagrangian cloud model. *Journal of Geophysical Research: Atmospheres*, *115*(D22).

Berner, A., Bretherton, C., & Wood, R. (2011). Large-eddy simulation of mesoscale dynamics and entrainment around a pocket of open cells observed in vocals-rex rf06. *Atmospheric Chemistry and Physics*, *11*(20), 10525–10540.

Berner, A., Bretherton, C., Wood, R., & Muhlbauer, A. (2013). Marine bound-

ary layer cloud regimes and poc formation in a crm coupled to a bulk aerosol scheme. *Atmospheric Chemistry and Physics*, *13*(24), 12549–12572.

Bower, K., Jones, A., & Choularton, T. (1999). A modelling study of aerosol processing by stratocumulus clouds and its impact on general circulation model parameterisations of cloud and aerosol. *Atmospheric research*, *50*(3-4), 317–344.

Bretherton, C., Blossey, P. N., & Uchida, J. (2007). Cloud droplet sedimentation, entrainment efficiency, and subtropical stratocumulus albedo. *Geophysical research letters*, *34*(3).

Bryan, G. H., & Fritsch, J. M. (2002). A benchmark simulation for moist nonhydrostatic numerical models. *Monthly Weather Review*, *130*(12), 2917–2928.

Chandrakar, K. K., Cantrell, W., Chang, K., Ciochetto, D., Niedermeier, D., Ovchinnikov, M., ... Yang, F. (2016). Aerosol indirect effect from turbulence-induced broadening of cloud-droplet size distributions. *Proceedings of the National Academy of Sciences*, *113*(50), 14243–14248.

Chandrakar, K. K., Cantrell, W., Ciochetto, D., Karki, S., Kinney, G., & Shaw, R. (2017). Aerosol removal and cloud collapse accelerated by supersaturation fluctuations in turbulence. *Geophysical Research Letters*, *44*(9), 4359–4367.

Chandrakar, K. K., Grabowski, W. W., Morrison, H., & Bryan, G. H. (2021). Impact of entrainment mixing and turbulent fluctuations on droplet size distributions in a cumulus cloud: An investigation using lagrangian microphysics with a subgrid-scale model. *Journal of the Atmospheric Sciences*, *78*(9), 2983–3005.

Chandrakar, K. K., Morrison, H., Grabowski, W. W., & Bryan, G. H. (2022). Comparison of lagrangian super-droplet and eulerian double-moment spectral microphysics schemes in large-eddy simulations of an isolated cumulus-congestus cloud. *Journal of the Atmospheric Sciences*.

Chandrakar, K. K., Morrison, H., & Witte, M. (2022). Evolution of droplet size distributions during the transition of an ultraclean stratocumulus cloud system to open cell structure: An les investigation using lagrangian microphysics. *Geophysical Research Letters*, *49*(17), e2022GL100511.

Chuang, P., Charlson, R. J., & Seinfeld, J. (1997). Kinetic limitations on droplet formation in clouds. *Nature*, *390*(6660), 594–596.

Deardorff, J. W. (1980). Stratocumulus-capped mixed layers derived from a three-dimensional model. *Boundary-layer meteorology*, *18*(4), 495–527.

Diamond, M. S., Gettelman, A., Lebsock, M. D., McComiskey, A., Russell, L. M., Wood, R., & Feingold, G. (2022). To assess marine cloud brightening's technical feasibility, we need to know what to study—and when to stop. *Proceedings of the National Academy of Sciences*, *119*(4), e2118379119.

Duynkerke, P. G., de Roode, S. R., van Zanten, M. C., Calvo, J., Cuxart, J., Cheinet, S., ... others (2004). Observations and numerical simulations of the diurnal cycle of the eurocs stratocumulus case. *Quarterly Journal of the Royal Meteorological Society: A journal of the atmospheric sciences, applied meteorology and physical oceanography*, *130*(604), 3269–3296.

Dziekan, P., Jensen, J. B., Grabowski, W. W., & Pawlowska, H. (2021). Impact of giant sea salt aerosol particles on precipitation in marine cumuli and stratocumuli: Lagrangian cloud model simulations. *Journal of the Atmospheric Sciences*, *78*(12), 4127–4142.

Erfani, E., Blossey, P., Wood, R., Mohrmann, J., Doherty, S. J., Wyant, M., & O, K.-T. (2022). Simulating aerosol lifecycle impacts on the subtropical stratocumulus-to-cumulus transition using large-eddy simulations. *Journal of Geophysical Research: Atmospheres*, *127*(21), e2022JD037258.

Feingold, G., Cotton, W. R., Kreidenweis, S. M., & Davis, J. T. (1999). The impact of giant cloud condensation nuclei on drizzle formation in stratocumulus: Implications for cloud radiative properties. *Journal of the atmospheric sciences*,

56(24), 4100–4117.

Feingold, G., Ghate, V. P., & Russell, L. M. (2022, 11). Doe-noaa marine cloud brightening workshop. *NOAA Technical Report OAR ESRL/CSL-1*. Retrieved from `https://www.osti.gov/biblio/1902730` doi: 10.2172/1902730

Feingold, G., & Kreidenweis, S. M. (2002). Cloud processing of aerosol as modeled by a large eddy simulation with coupled microphysics and aqueous chemistry. *Journal of Geophysical Research: Atmospheres*, *107*(D23), AAC–6.

Feingold, G., Tzivion, S., & Leviv, Z. (1988). Evolution of raindrop spectra. part i: Solution to the stochastic collection/breakup equation using the method of moments. *Journal of Atmospheric Sciences*, *45*(22), 3387–3399.

Glassmeier, F., & Feingold, G. (2017). Network approach to patterns in stratocumulus clouds. *Proceedings of the National Academy of Sciences*, *114*(40), 10578–10583.

Glassmeier, F., Hoffmann, F., Johnson, J. S., Yamaguchi, T., Carslaw, K. S., & Feingold, G. (2021). Aerosol-cloud-climate cooling overestimated by ship-track data. *Science*, *371*(6528), 485–489.

Goren, T., Kazil, J., Hoffmann, F., Yamaguchi, T., & Feingold, G. (2019). Anthropogenic air pollution delays marine stratocumulus breakup to open cells. *Geophysical Research Letters*, *46*(23), 14135–14144.

Goren, T., & Rosenfeld, D. (2012). Satellite observations of ship emission induced transitions from broken to closed cell marine stratocumulus over large areas. *Journal of Geophysical Research: Atmospheres*, *117*(D17).

Goren, T., & Rosenfeld, D. (2015). Extensive closed cell marine stratocumulus downwind of europe—a large aerosol cloud mediated radiative effect or forcing? *Journal of Geophysical Research: Atmospheres*, *120*(12), 6098–6116.

Grabowski, W. W., Morrison, H., Shima, S.-I., Abade, G. C., Dziekan, P., & Pawlowska, H. (2019). Modeling of cloud microphysics: Can we do better? *Bulletin of the American Meteorological Society*, *100*(4), 655–672.

Hill, A., Dobbie, S., & Yin, Y. (2008). The impact of aerosols on non-precipitating marine stratocumulus. i: Model description and prediction of the indirect effect. *Quarterly Journal of the Royal Meteorological Society: A journal of the atmospheric sciences, applied meteorology and physical oceanography*, *134*(634), 1143–1154.

Hoffmann, F., & Feingold, G. (2023). A note on aerosol processing by droplet collision-coalescence. *Geophysical Research Letters*, *50*(11), e2023GL103716.

Hoppel, W., Fitzgerald, J., Frick, G., Larson, R., & Mack, E. (1990). Aerosol size distributions and optical properties found in the marine boundary layer over the atlantic ocean. *Journal of Geophysical Research: Atmospheres*, *95*(D4), 3659–3686.

Hudson, J. G., Noble, S., & Tabor, S. (2015). Cloud supersaturations from ccn spectra hoppel minima. *Journal of Geophysical Research: Atmospheres*, *120*(8), 3436–3452.

Kazil, J., Wang, H., Feingold, G., Clarke, A., Snider, J. R., & Bandy, A. (2011). Modeling chemical and aerosol processes in the transition from closed to open cells during vocals-rex. *Atmospheric Chemistry and Physics*, *11*(15), 7491–7514.

Latham, J., Rasch, P., Chen, C.-C., Kettles, L., Gadian, A., Gettelman, A., ... Choularton, T. (2008). Global temperature stabilization via controlled albedo enhancement of low-level maritime clouds. *Philosophical Transactions of the Royal Society A: Mathematical, Physical and Engineering Sciences*, *366*(1882), 3969–3987.

Lee, H., Fridlind, A. M., & Ackerman, A. S. (2021). An evaluation of size-resolved cloud microphysics scheme numerics for use with radar observations. part ii: Condensation and evaporation. *Journal of the Atmospheric Sciences*, *78*(5), 1629–1645.

Magaritz, L., Pinsky, M., Krasnov, O., & Khain, A. (2009). Investigation of droplet size distributions and drizzle formation using a new trajectory ensemble model. part ii: Lucky parcels. *Journal of the atmospheric sciences*, *66*(4), 781–805.

Mechem, D. B., & Kogan, Y. L. (2003). Simulating the transition from drizzling marine stratocumulus to boundary layer cumulus with a mesoscale model. *Monthly weather review*, *131*(10), 2342–2360.

Mechem, D. B., Robinson, P. C., & Kogan, Y. L. (2006). Processing of cloud condensation nuclei by collision-coalescence in a mesoscale model. *Journal of Geophysical Research: Atmospheres*, *111*(D18).

Mellado, J.-P., Bretherton, C., Stevens, B., & Wyant, M. (2018). Dns and les for simulating stratocumulus: Better together. *Journal of Advances in Modeling Earth Systems*, *10*(7), 1421–1438.

Morrison, H., Witte, M., Bryan, G. H., Harrington, J. Y., & Lebo, Z. J. (2018). Broadening of modeled cloud droplet spectra using bin microphysics in an eulerian spatial domain. *Journal of the Atmospheric Sciences*, *75*(11), 4005–4030.

Pierce, J., Croft, B., Kodros, J., D'Andrea, S., & Martin, R. (2015). The importance of interstitial particle scavenging by cloud droplets in shaping the remote aerosol size distribution and global aerosol-climate effects. *Atmospheric Chemistry and Physics*, *15*(11), 6147–6158.

Pincus, R., & Baker, M. B. (1994). Effect of precipitation on the albedo susceptibility of clouds in the marine boundary layer. *Nature*, *372*(6503), 250–252.

Pinsky, M., Magaritz, L., Khain, A., Krasnov, O., & Sterkin, A. (2008). Investigation of droplet size distributions and drizzle formation using a new trajectory ensemble model. part i: Model description and first results in a nonmixing limit. *Journal of the atmospheric sciences*, *65*(7), 2064–2086.

Reutter, P., Su, H., Trentmann, J., Simmel, M., Rose, D., Gunthe, S., ... Pöschl, U. (2009). Aerosol-and updraft-limited regimes of cloud droplet formation: influence of particle number, size and hygroscopicity on the activation of cloud condensation nuclei (ccn). *Atmospheric Chemistry and Physics*, *9*(18), 7067–7080.

Rosenfeld, D., Kaufman, Y., & Koren, I. (2006). Switching cloud cover and dynamical regimes from open to closed benard cells in response to the suppression of precipitation by aerosols. *Atmospheric Chemistry and Physics*, *6*(9), 2503–2511.

Savic-Jovcic, V., & Stevens, B. (2008). The structure and mesoscale organization of precipitating stratocumulus. *Journal of the Atmospheric Sciences*, *65*(5), 1587–1605.

Seinfeld, J. H., & Pandis, S. N. (1998). From air pollution to climate change. *Atmospheric chemistry and physics*, *1326*.

Seinfeld, J. H., & Pandis, S. N. (2016). *Atmospheric chemistry and physics: from air pollution to climate change*. John Wiley & Sons.

Sharon, T. M., Albrecht, B. A., Jonsson, H. H., Minnis, P., Khaiyer, M. M., van Reken, T. M., ... Flagan, R. (2006). Aerosol and cloud microphysical characteristics of rifts and gradients in maritime stratocumulus clouds. *Journal of the atmospheric sciences*, *63*(3), 983–997.

Shima, S.-i., Kusano, K., Kawano, A., Sugiyama, T., & Kawahara, S. (2009). The super-droplet method for the numerical simulation of clouds and precipitation: A particle-based and probabilistic microphysics model coupled with a non-hydrostatic model. *Quarterly Journal of the Royal Meteorological Society: A journal of the atmospheric sciences, applied meteorology and physical oceanography*, *135*(642), 1307–1320.

Shima, S.-i., Sato, Y., Hashimoto, A., & Misumi, R. (2020). Predicting the morphology of ice particles in deep convection using the super-droplet method: development and evaluation of scale-sdm 0.2. 5-2.2. 0,-2.2. 1, and-2.2. 2. *Geo-*

scientific Model Development, *13*(9), 4107–4157.

Slingo, A. (1990). Sensitivity of the earth's radiation budget to changes in low clouds. *Nature*, *343*(6253), 49–51.

Stevens, B., Feingold, G., Cotton, W. R., & Walko, R. L. (1996). Elements of the microphysical structure of numerically simulated nonprecipitating stratocumulus. *Journal of Atmospheric Sciences*, *53*(7), 980–1006.

Stevens, B., Moeng, C.-H., Ackerman, A. S., Bretherton, C. S., Chlond, A., de Roode, S., ... others (2005). Evaluation of large-eddy simulations via observations of nocturnal marine stratocumulus. *Monthly weather review*, *133*(6), 1443–1462.

Twomey, S. (1974). Pollution and the planetary albedo. *Atmospheric Environment (1967)*, *8*(12), 1251–1256.

Tzivion, S., Feingold, G., & Levin, Z. (1987). An efficient numerical solution to the stochastic collection equation. *Journal of Atmospheric Sciences*, *44*(21), 3139–3149.

Wang, H., & Feingold, G. (2009). Modeling mesoscale cellular structures and drizzle in marine stratocumulus. part i: Impact of drizzle on the formation and evolution of open cells. *Journal of the Atmospheric Sciences*, *66*(11), 3237–3256.

Wood, R. (2012). Stratocumulus clouds. *Monthly Weather Review*, *140*(8), 2373–2423.

Wood, R., Bretherton, C., Leon, D., Clarke, A., Zuidema, P., Allen, G., & Coe, H. (2011). An aircraft case study of the spatial transition from closed to open mesoscale cellular convection over the southeast pacific. *Atmospheric Chemistry and Physics*, *11*(5), 2341–2370.

Wood, R., Comstock, K., Bretherton, C. S., Cornish, C., Tomlinson, J., Collins, D. R., & Fairall, C. (2008). Open cellular structure in marine stratocumulus sheets. *Journal of Geophysical Research: Atmospheres*, *113*(D12).

Zhang, S., Wang, M., Ghan, S. J., Ding, A., Wang, H., Zhang, K., ... others (2016). On the characteristics of aerosol indirect effect based on dynamic regimes in global climate models. *Atmospheric Chemistry and Physics*, *16*(5), 2765–2783.

Figure 1.

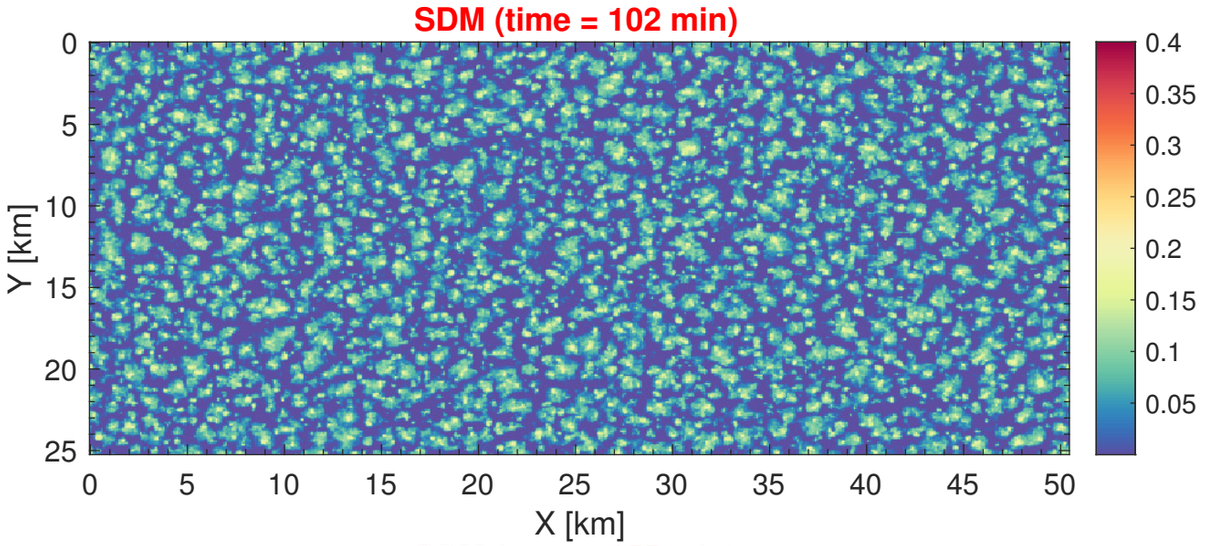
SDM (time = 102 min)
Y [km]
X [km]

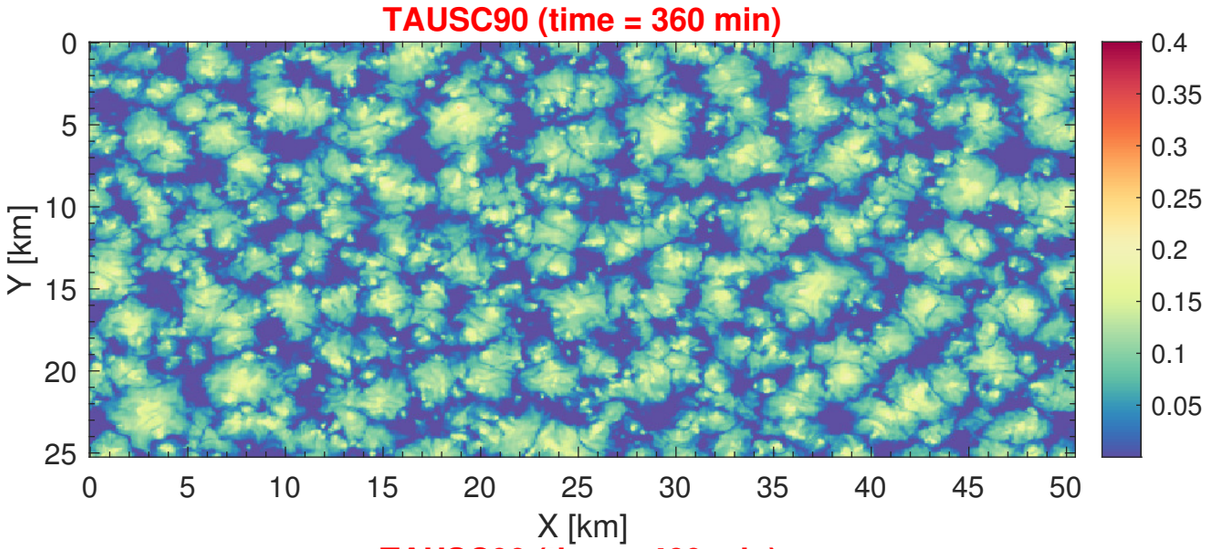
TAUSC90 (time = 360 min)
Y [km]
X [km]

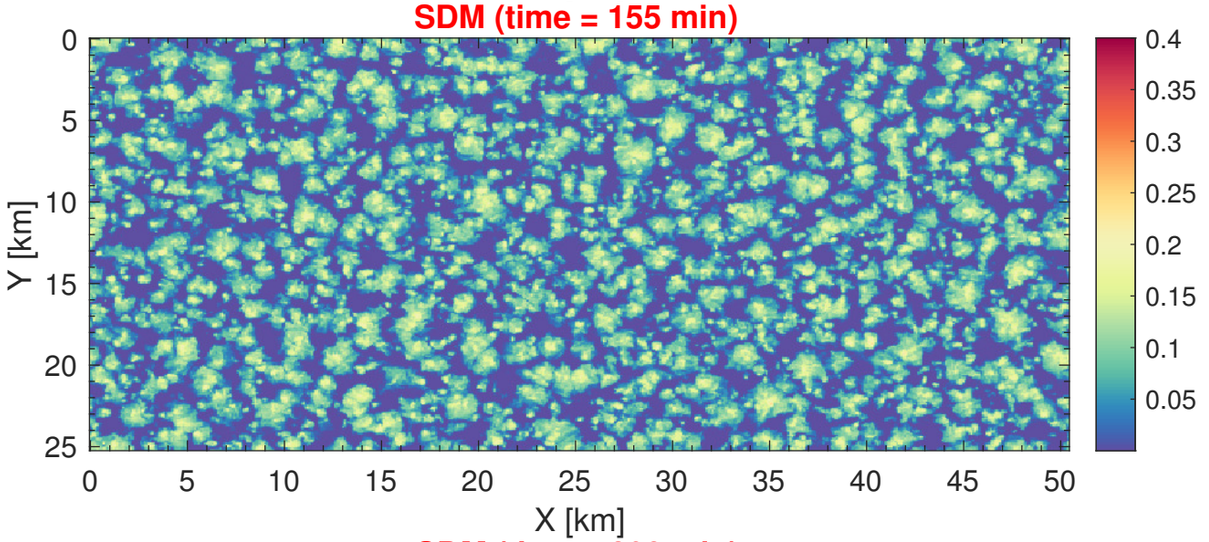
SDM (time = 155 min)
Y [km]
X [km]

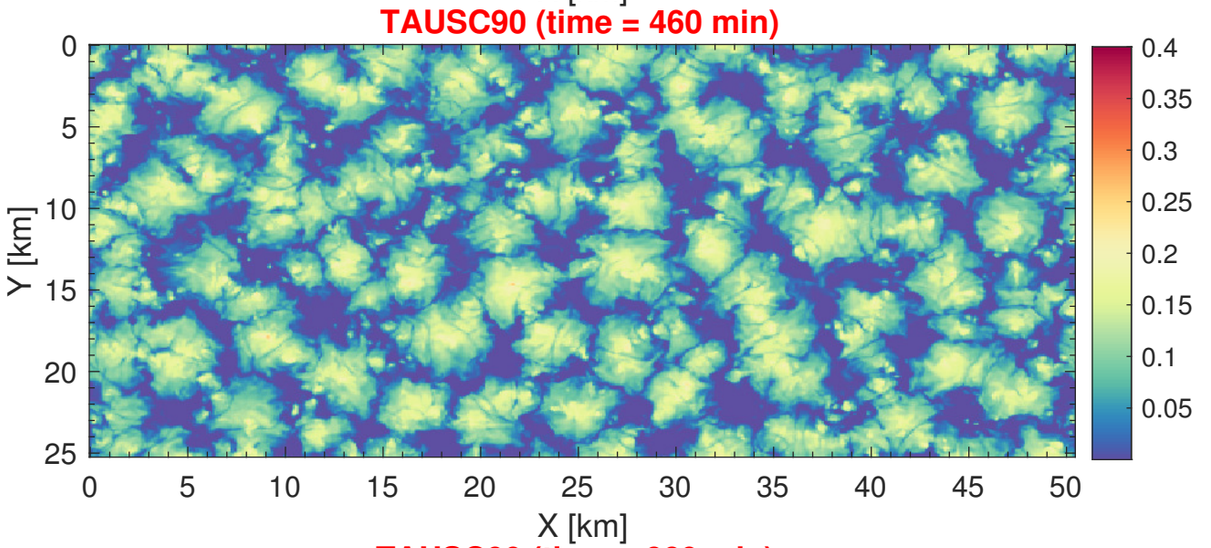
TAUSC90 (time = 460 min)
Y [km]
X [km]

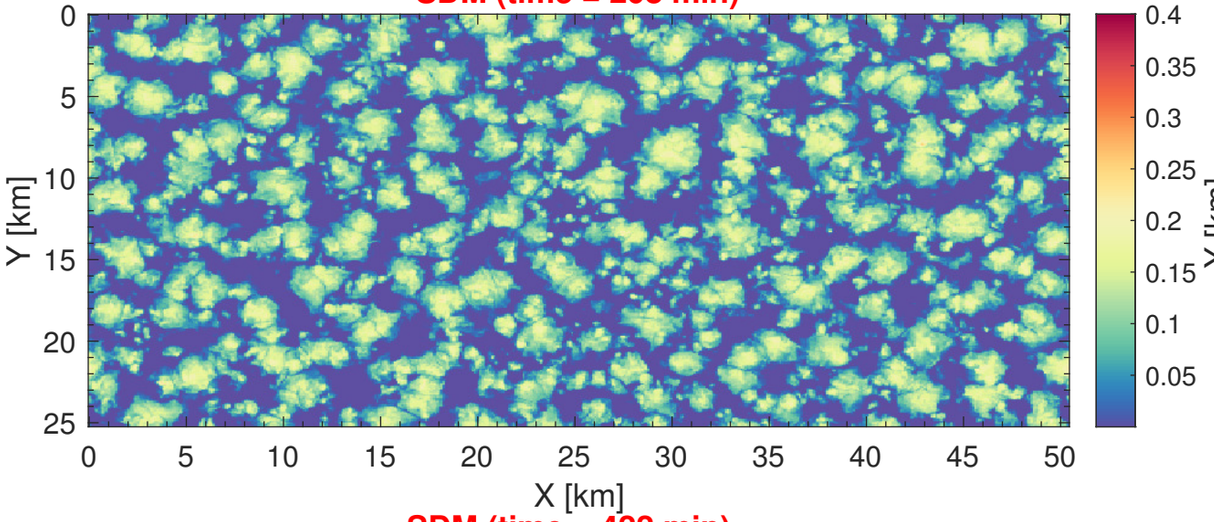
SDM (time = 208 min)
Y [km]
X [km]

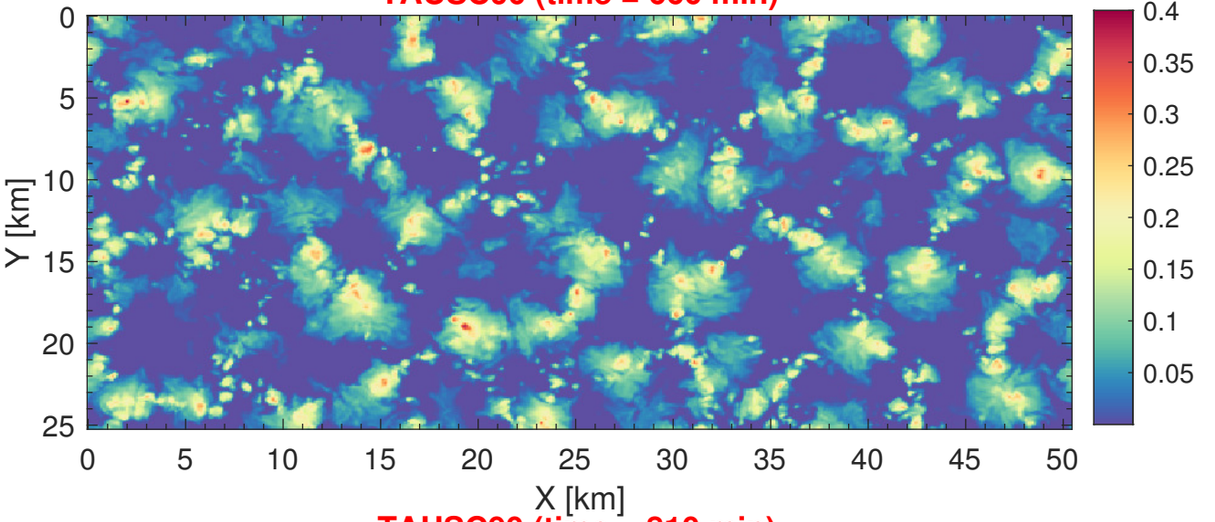
TAUSC90 (time = 660 min)
Y [km]
X [km]

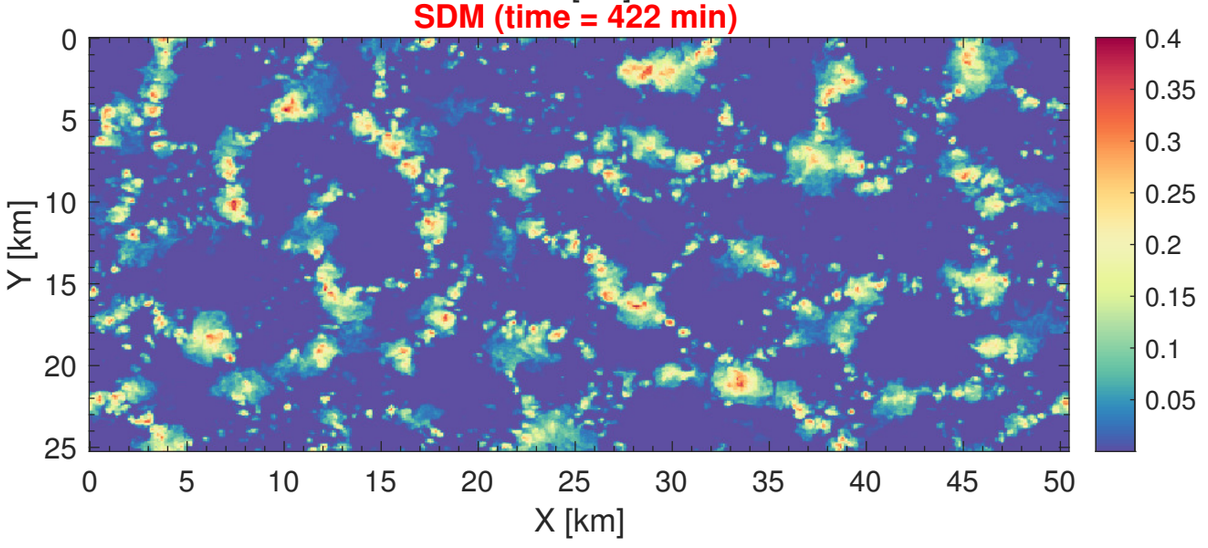
SDM (time = 422 min)
Y [km]
X [km]

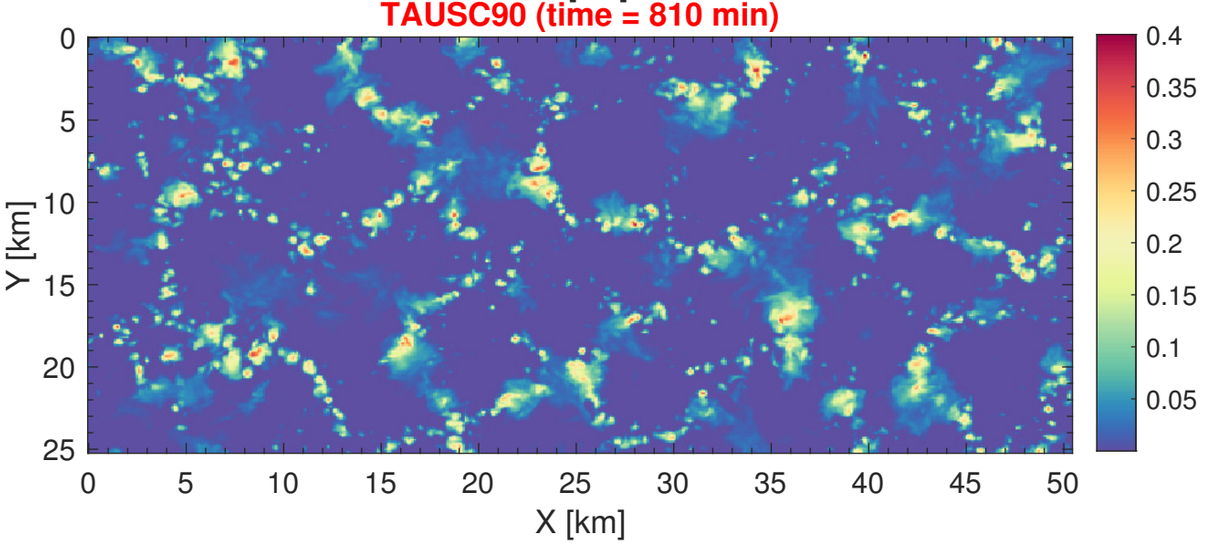
TAUSC90 (time = 810 min)
Y [km]
X [km]

Figure 2.

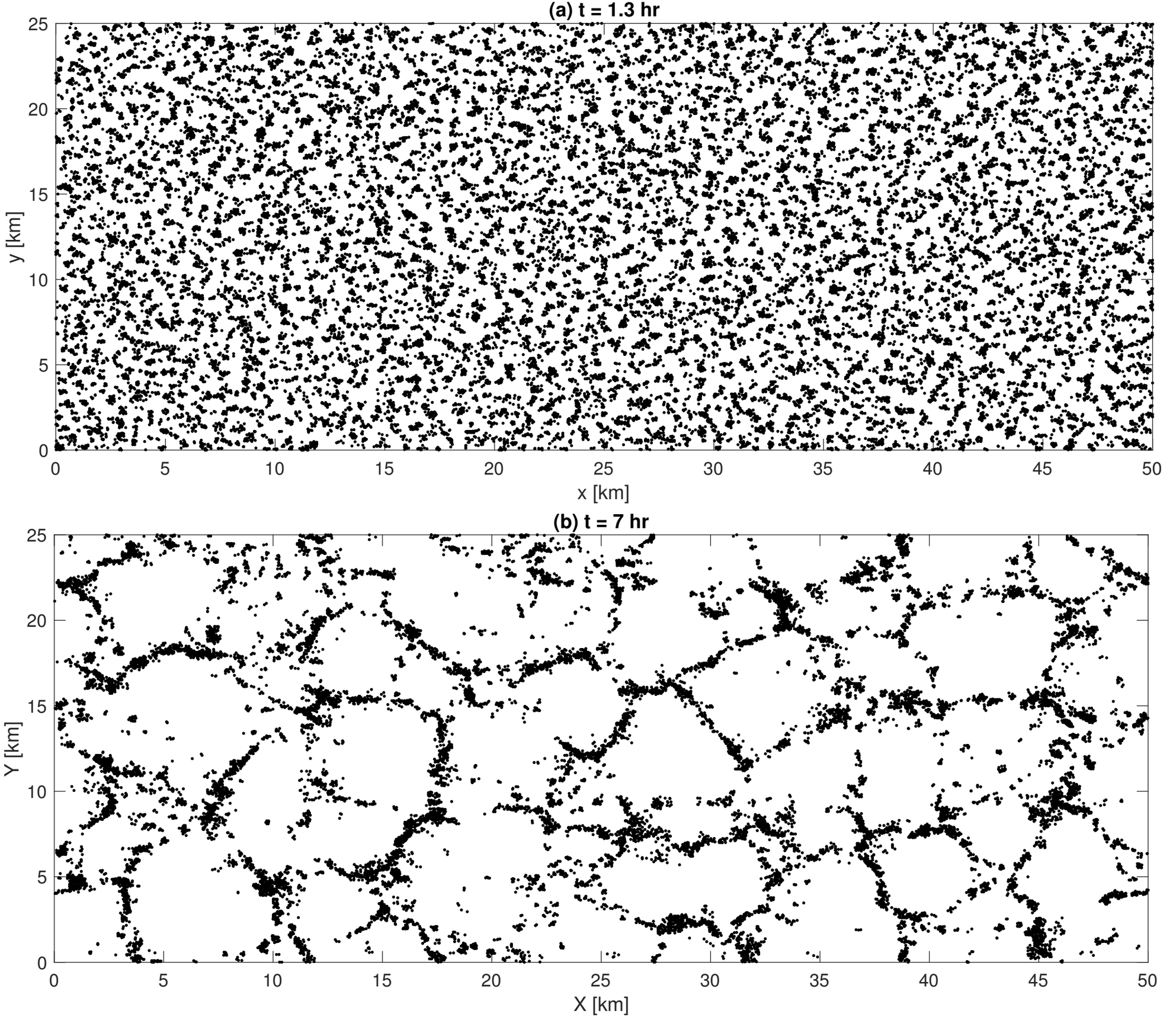
(a) t = 1.3 hr
y [km]
x [km]
0
5
10
15
20
25
30
35
40
45
50
(b) t = 7 hr
Y [km]
X [km]

Figure 3.

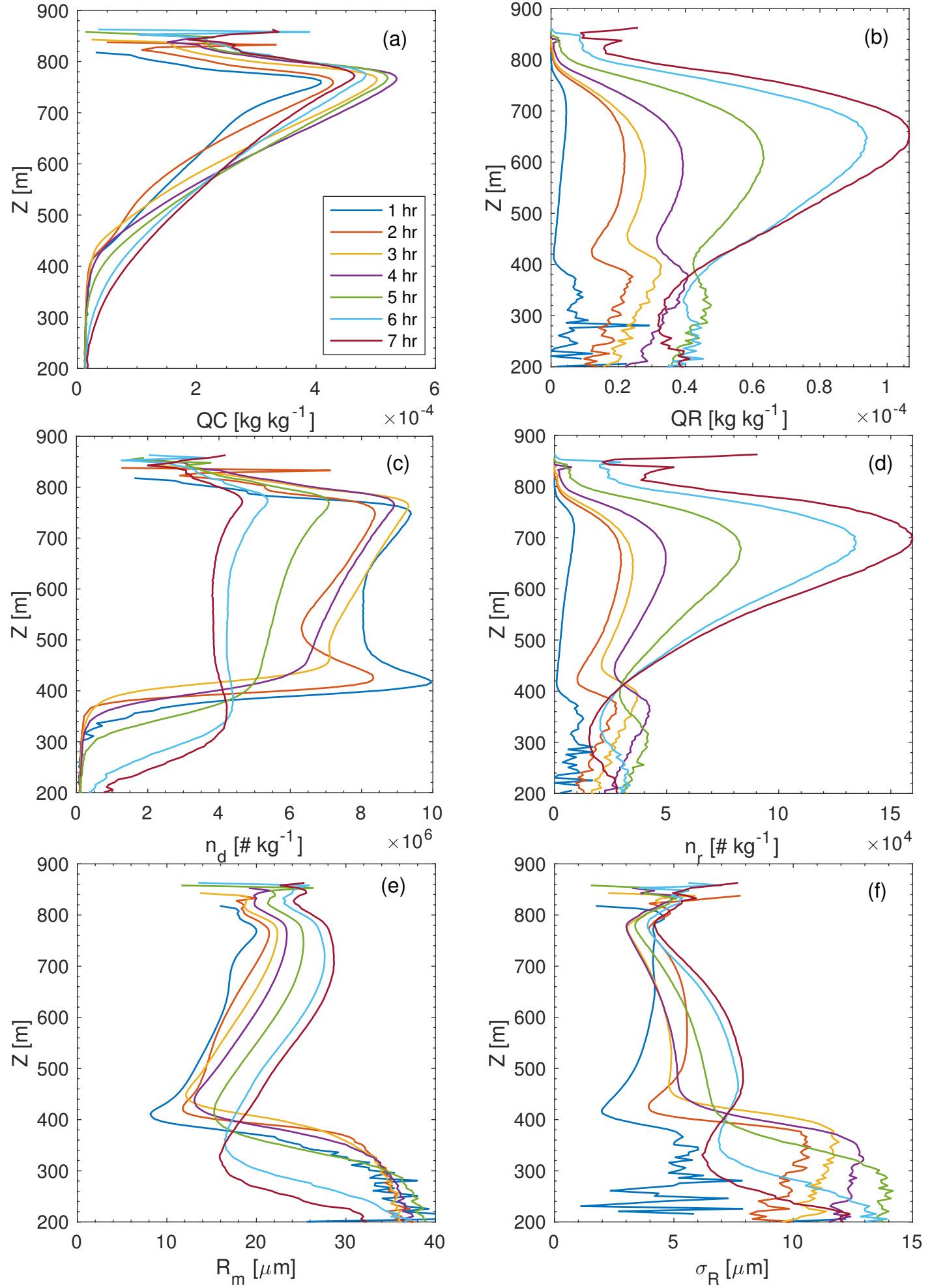
(a)
(b)
(c)
(d)
(e)
(f)
Z [m]
QC [kg kg^{-1}]
$\times 10^{-4}$
QR [kg kg^{-1}]
$\times 10^{-4}$
n_d [# kg^{-1}]
$\times 10^{6}$
n_r [# kg^{-1}]
$\times 10^{4}$
R_m [μm]
σ_R [μm]
1 hr
2 hr
3 hr
4 hr
5 hr
6 hr
7 hr

Figure 4.

PDF

10^{0}
10^{-1}
10^{-2}
10^{-3}
10^{-4}
10^{-5}
10^{-6}

200m< Z <250m
255m< Z <305m
310m< Z <360m
365m< Z <415m
420m< Z <470m
475m< Z <525m
530m< Z <580m
585m< Z <635m
640m< Z <690m
695m< Z <745m
750m< Z <800m
Background (time = 0 hours

10^{1}
10^{2}
10^{3}

R_a [nm]

Figure 5.

(a) Only cloudy grid cells

TAUSC90
SDM
TAUSC80
TAUSC70
TAU-AERO-HI-PROC
TAU-AERO-LO-PROC
TAU-AERO-LO

Aerosol Mixing Ratio [mg^{-1}]

t [hr]

(b) In the bounday layer
(upto the average cloud top)

Aerosol Mixing Ratio [mg^{-1}]

t [hr]

Figure 6 Part-I.

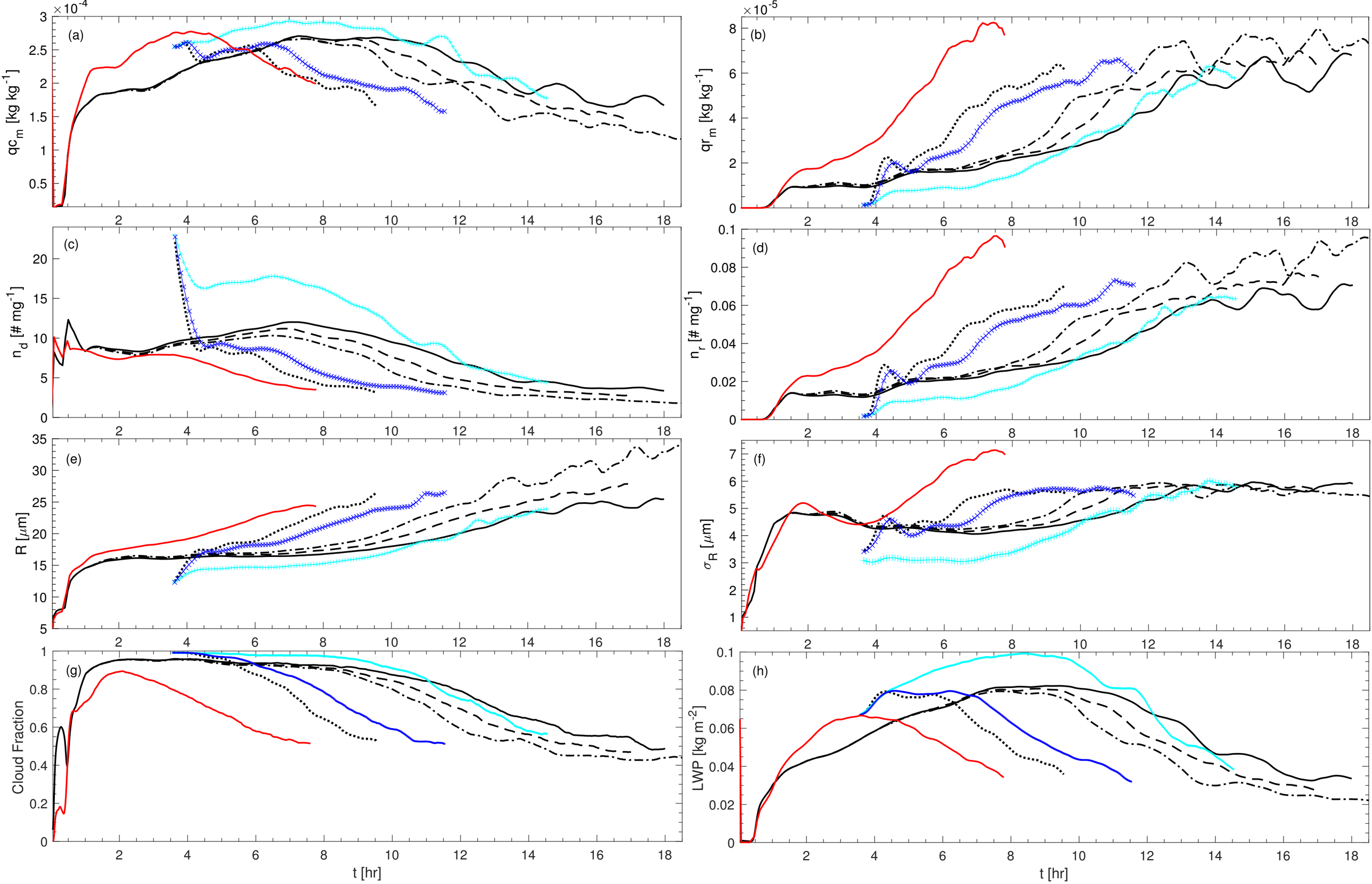
(a)
qc_m [kg kg^{-1}]
$\times 10^{-4}$
(b)
qr_m [kg kg^{-1}]
$\times 10^{-5}$
(c)
n_d [# mg^{-1}]
(d)
n_r [# mg^{-1}]
(e)
R [μm]
(f)
σ_R [μm]
(g)
Cloud Fraction
(h)
LWP [kg m^{-2}]
t [hr]

Figure 6 Part-II.

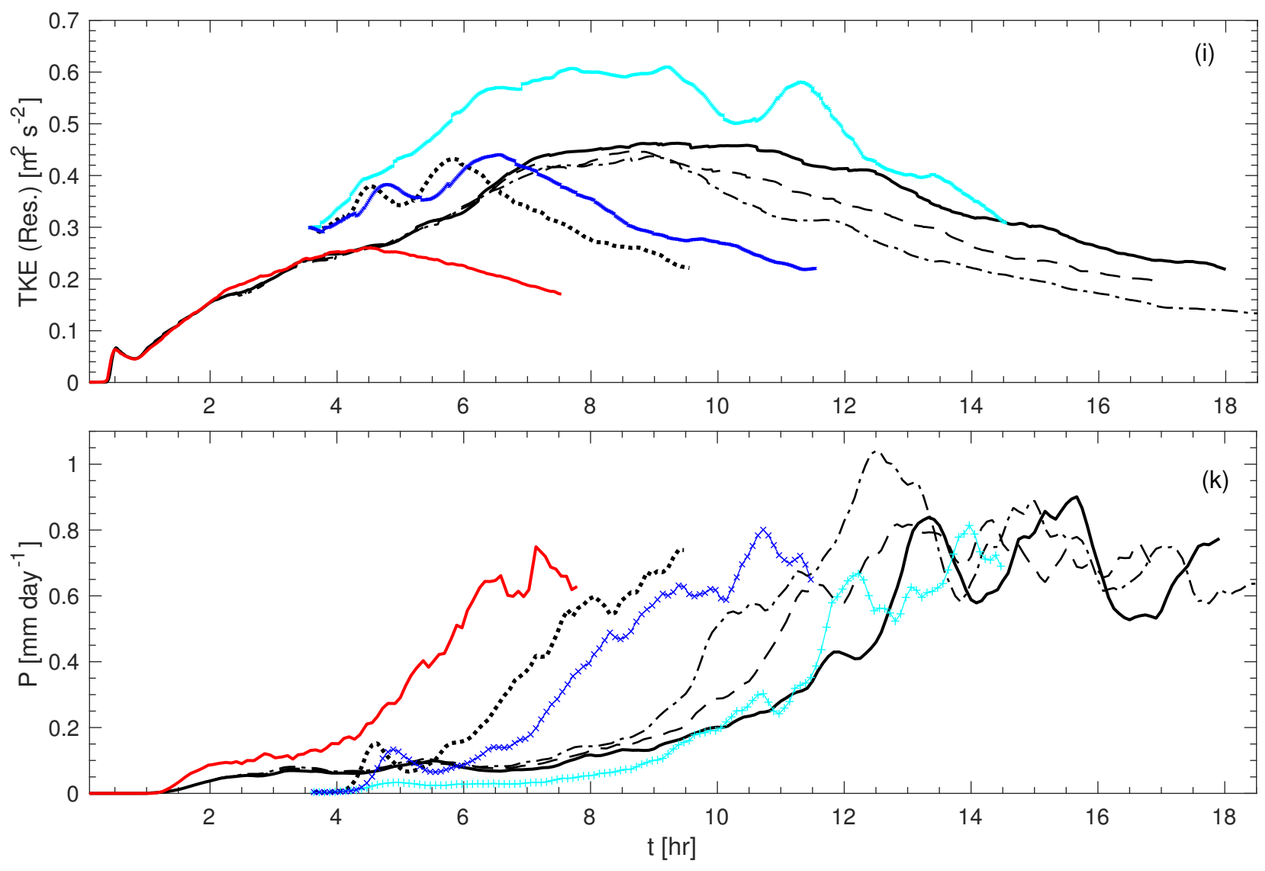
(i)
TKE (Res.) [m^2 s^{-2}]
0
0.1
0.2
0.3
0.4
0.5
0.6
0.7
2
4
6
8
10
12
14
16
18

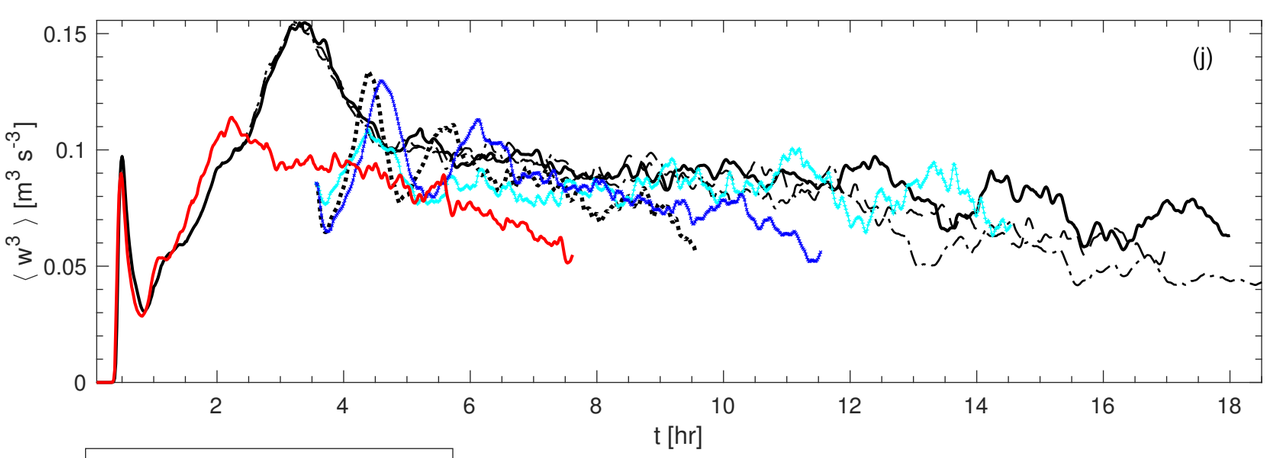
(j)
⟨ w^3 ⟩ [m^3 s^{-3}]
0
0.05
0.1
0.15
2
4
6
8
10
12
14
16
18
t [hr]

(k)
P [mm day^{-1}]
0
0.2
0.4
0.6
0.8
1
2
4
6
8
10
12
14
16
18
t [hr]

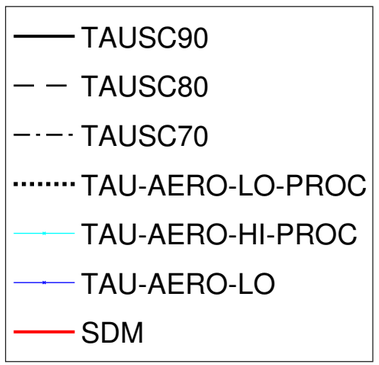
TAUSC90
TAUSC80
TAUSC70
TAU-AERO-LO-PROC
TAU-AERO-HI-PROC
TAU-AERO-LO
SDM

Figure 7.

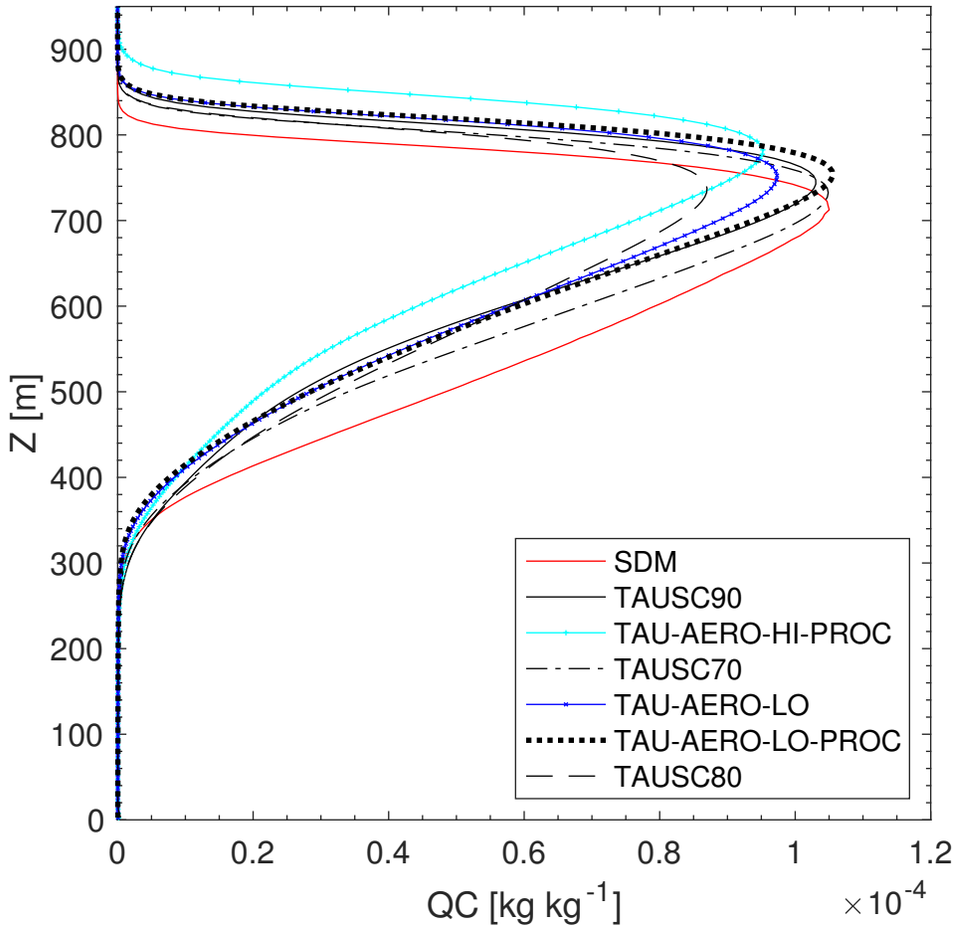
Z [m]
QC [kg kg^{-1}]
$\times 10^{-4}$
SDM
TAUSC90
TAU-AERO-HI-PROC
TAUSC70
TAU-AERO-LO
TAU-AERO-LO-PROC
TAUSC80

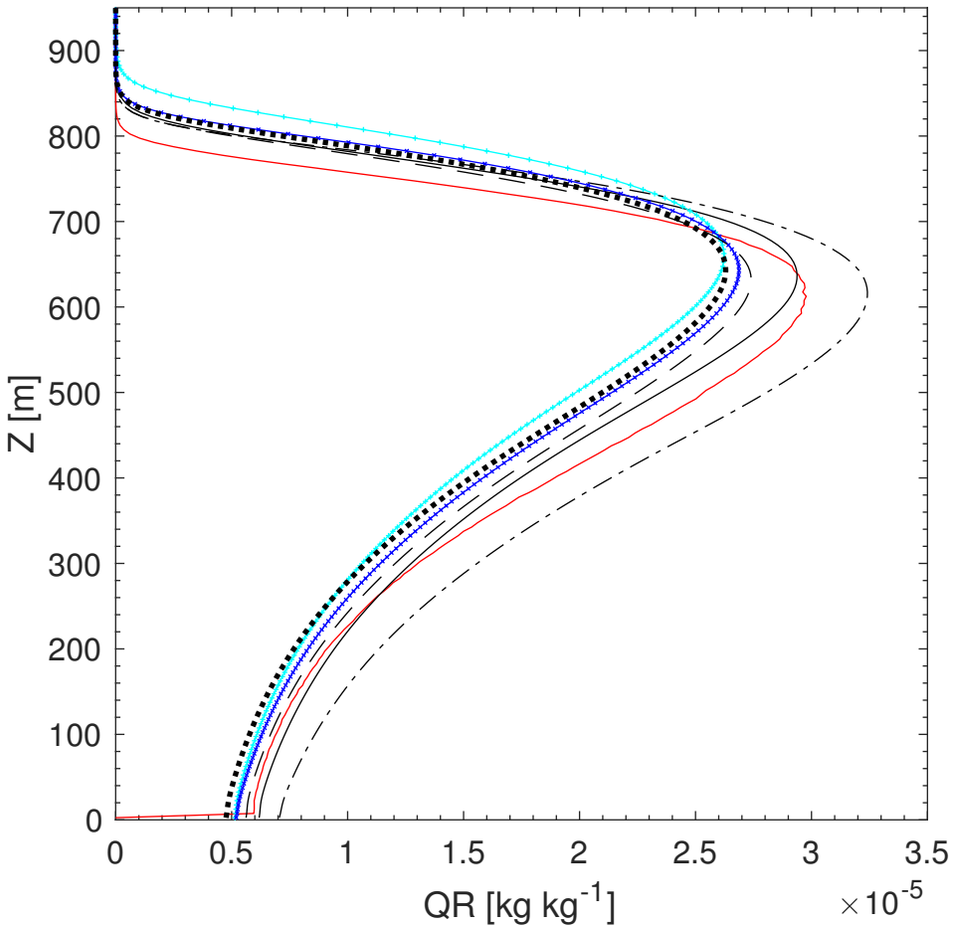
Z [m]
QR [kg kg^{-1}]
$\times 10^{-5}$

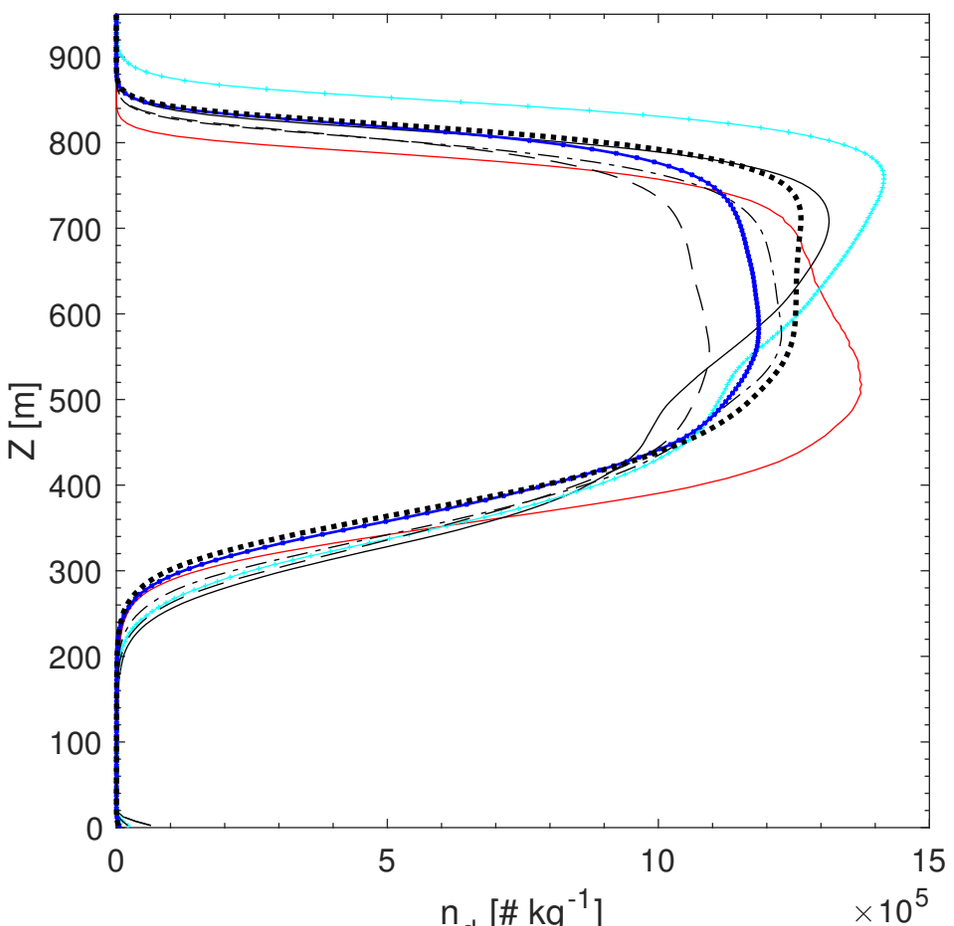
Z [m]
n_d [# kg^{-1}]
$\times 10^{5}$

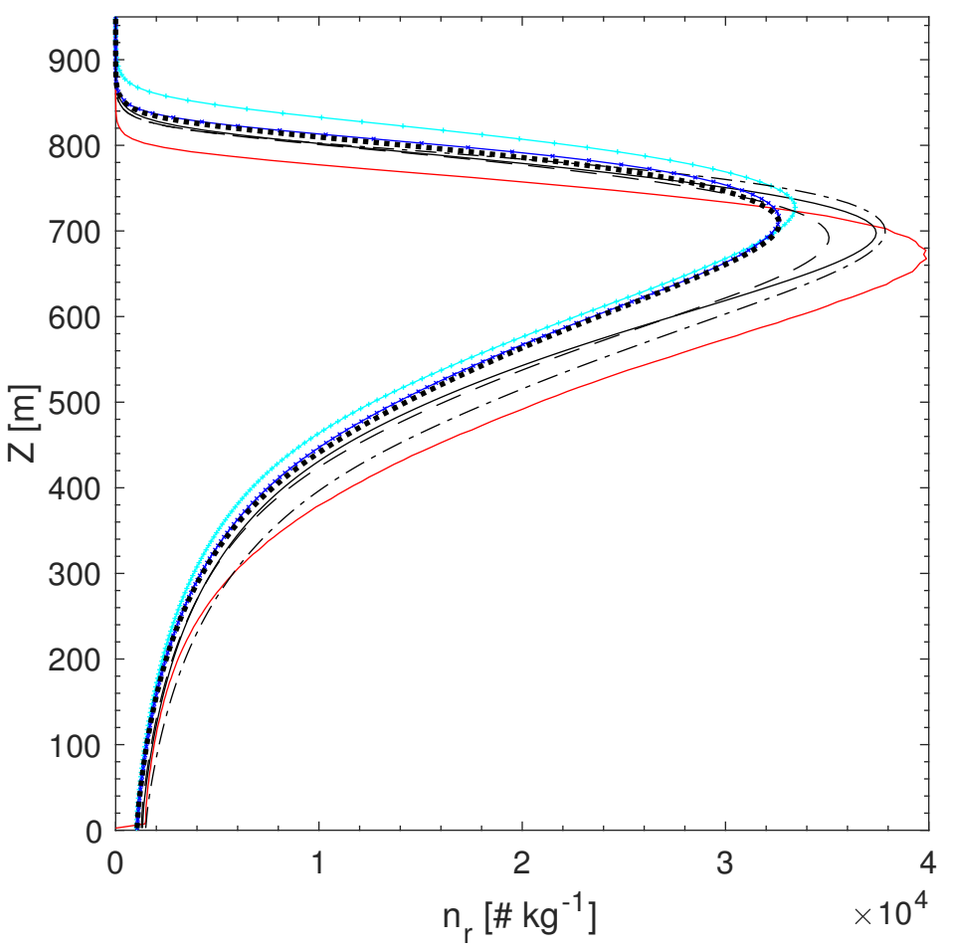
Z [m]
n_r [# kg^{-1}]
$\times 10^{4}$

Figure 8.

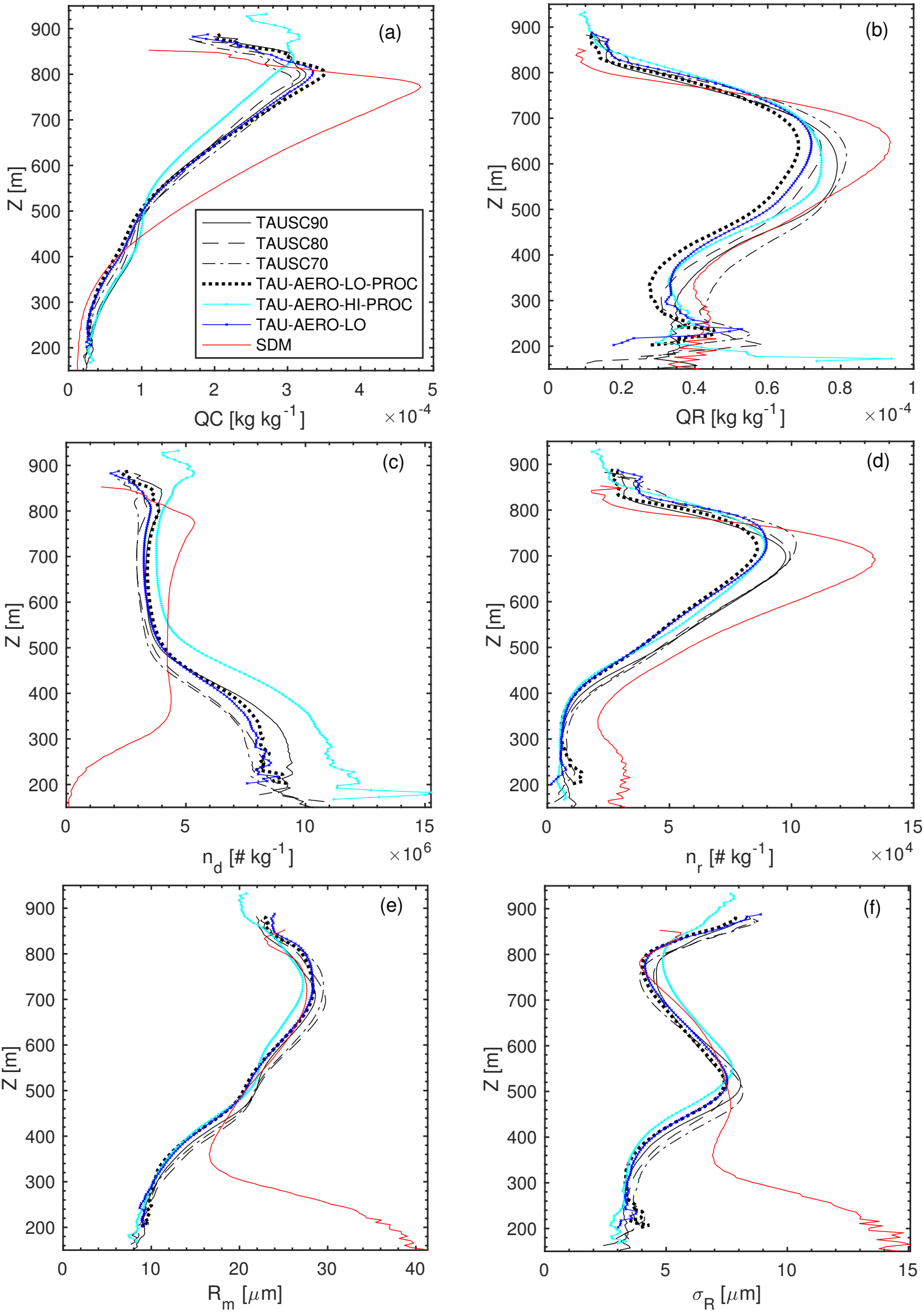
(a)
(b)
(c)
(d)
(e)
(f)
Z [m]
QC [kg kg^{-1}]
$\times 10^{-4}$
QR [kg kg^{-1}]
$\times 10^{-4}$
n_d [# kg^{-1}]
$\times 10^{6}$
n_r [# kg^{-1}]
$\times 10^{4}$
R_m [μm]
σ_R [μm]
TAUSC90
TAUSC80
TAUSC70
TAU-AERO-LO-PROC
TAU-AERO-HI-PROC
TAU-AERO-LO
SDM